NASA Technical Memorandum 110423

Helicopter Blade-Vortex Interaction Noise with Comparisons to CFD Calculations

Megan S McCluer

December 1996

National Aeronautics and
Space Administration

Space Administration

Contents

List of Tables

List of Figures

Nomenclature

All quantities are nondimensionalized by the rotor blade chord, and/or the freestream speed of sound, unless otherwise noted.

A, B, C	Jacobian matrices
a_0	Vortex core radius, nondimensional
c	Chord of rotor blade (in.)
C	Chord of the vortex generator (in.)
dB	Decibels
E, F, G	Inviscid flux vectors
e	Total energy per unit volume
H_t	Total enthalpy
i, j, k	Integer coordinate directions
J	Transformation Jacobian
M_{tip}	Hover tip Mach number
p	Static pressure, nondimensionalized by dynamic pressure
P	Newton sub-iteration number
Q	Vector of conserved quantities
Q_L, Q_R	Left and right hand conserved quantity variables
r	Radial distance from the vortex center, nondimensional
t,	Time (sec)
U_∞	Freestream velocity (ft/s)
U, V, W	Contravariant velocities
u, v, w	Velocity components in physical space
x, y, z	Physical space coordinates
Z_v	Separation distance between vortex and rotor, nondimensional
α	Angle of attack (deg)
α_v	Angle of attack of vortex generator (deg)
ε	Small constant ($\sim 10^{-6}$)
$\hat{\Gamma}$	Vortex strength, nondimensional, ($\hat{\Gamma} = \Gamma/U_\infty C$)
κ	Parameter controlling order of scheme
ρ	Density
γ	Ratio of specific heats
μ	Advance ratio
ξ, η, ζ	Transformed curvilinear coordinates
σ	Spectral radius
τ	Time, nondimensional
Ω	Angular velocity of rotor blade (rpm)
ψ	Azimuth angle (deg)

Helicopter Blade-Vortex Interaction Noise with Comparisons to CFD Calculations

MEGAN S MCCLUER

Ames Research Center

Summary

A comparison of experimental acoustics data and computational predictions was performed for a helicopter rotor blade interacting with a parallel vortex. The experiment was designed to examine the aerodynamics and acoustics of parallel blade-vortex interaction (BVI) and was performed in the Ames Research Center (ARC) 80- by 120-Foot Subsonic Wind Tunnel. An independently generated vortex interacted with a small-scale, nonlifting helicopter rotor at the 180 deg azimuth angle to create the interaction in a controlled environment. Computational fluid dynamics (CFD) was used to calculate near-field pressure time histories. The CFD code, called Transonic Unsteady Rotor Navier–Stokes (TURNS), was used to make comparisons with the acoustic pressure measurement at two microphone locations and several test conditions. The test conditions examined included hover tip Mach numbers of 0.6 and 0.7, advance ratio of 0.2, positive and negative vortex rotation, and the vortex passing above and below the rotor blade by 0.25 rotor chords. The results show that the CFD qualitatively predicts the acoustic characteristics very well, but quantitatively overpredicts the peak-to-peak sound pressure level by 15 percent in most cases. There also exists a discrepancy in the phasing (about 4 deg) of the BVI event in some cases. Additional calculations were performed to examine the effects of vortex strength, thickness, time accuracy, and directionality. This study validates the TURNS code for prediction of near-field acoustic pressures of controlled parallel BVI.

1 Introduction

Rotorcraft have been consistently designed with performance and productivity as driving goals, and external acoustics has not previously been a primary concern. The result has typically been well-performing and productive aircraft, yet with high and sometimes excessive noise levels. Community concern of noise pollution and military concern of detectability have motivated Federal Aviation Administration (FAA) and military certification authorities to require significant reductions in noise levels. In response, rigorous research into rotorcraft acoustics has been initiated to better understand the noise sources of rotary-wing aircraft. If the sources of noise generated by helicopters can be sufficiently understood, then computational models may be developed with the ultimate goal to allow engineers to predict noise and take steps to minimize obtrusive noise early in the design process.

Currently, many different types of computational models are still being refined, and comparisons with experimental data are necessary to ensure that the predicted acoustics is accurate. This type of comparison (comparing a computational model with measured data), is the primary subject of this paper.

A wind tunnel test was performed that was specifically designed to acquire helicopter rotor acoustics data suitable for comparison with computational codes. This study will discuss the experiment and the procedures that were used to acquire, process, and analyze the experimental acoustics data in the near-field. The experimental results of eight test cases are presented. An existing Euler/Navier–Stokes code, described in section 3, was used to perform calculations that simulated the experiment. The calculated results were processed and compared to the measured results from the wind tunnel experiment. Additional data were extracted from the computations to study various phenomena, such as the tendency for blade-vortex interaction (BVI) noise to propagate in a specific direction.

This introductory section discusses helicopter main rotor noise sources, and explains why BVI noise is the main subject of this study.

1.1 Rotorcraft Aeroacoustics

The aerodynamic environment of helicopter rotor blades is extremely complicated due to the combination of rotation of the blades and the translation of the helicopter. This is further complicated by the main rotor wake interacting with the fuselage and tail. These various unsteady aerodynamic interactions, as well as the transmission, engine and tail rotor, all generate noise. Figure 1.1 illustrates typical aerodynamic interactions that can occur

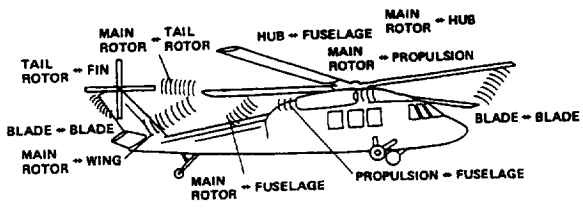

Figure 1.1 Examples of aerodynamic interactions of a helicopter that are possible noise sources.

on a helicopter. The far-field acoustic signature of a helicopter is mostly dominated by the changing aerodynamic environment of the main rotor blades.

Main rotor aeroacoustic phenomena are generally classified into four main types; broadband noise, rotational noise, high speed impulsive noise, and BVI noise. When BVI noise occurs, it is highly impulsive and generally dominates the other sources of noise. Before discussing BVI noise, it is helpful to understand the other sources of noise.

1.1.1 Broadband noise– Broadband noise is sound produced by random fluctuations of the forces on the blades and is evident throughout a wide range of frequencies. This is noise generated by a turbulent flow environment, which is caused by turbulence in the ambient atmosphere and the turbulent wakes of preceding rotor blades. The unsteady loading on the blades due to these interactions, which are randomly distributed in time and location, produces a continual addition of sound power to the time history, and has no distinct frequencies dominating the spectrum. The sound energy is distributed over a substantial portion of the spectrum, from about 150 to 1000 Hz (ref. 1). Broadband noise is usually significantly lower in amplitude than the other noise sources, which are described below.

1.1.2 Rotational noise– Rotational noise is sound created by the rotor blades exerting a force on the air, such as when the blades are generating lift. The steady and varying loads on the rotor blades, as they rotate around the azimuth, creates this low frequency noise source. The loading noise due to the harmonic blade airloads dominate the rotational noise at low rotor blade tip Mach numbers ($M_{tip} < 0.5$ to 0.7) (ref. 2). Lift and drag forces contribute to noise directed out-of-plane and in-plane of the rotor, respectively. [In general, steady forces on a rotating blade (lift and drag) radiate in a dipole nature. Steady thickness sources are monopole and stresses in the fluid are quadropole in nature.]

Since low frequencies propagate well in air, rotational noise can make rotorcraft detectable from long distances. Rotational noise can also be a source of vibration and acoustically induced structural fatigue on the vehicle. The time history of isolated rotational noise shows smooth rolling humps at the blade passage frequency. The sound power spectrum has peaks at the rotational frequency and higher harmonics. Figure 1.2 is a frequency spectrum of a typical helicopter far-field noise signature. It can be seen that the main rotor rotational frequency and its harmonics dominate the sound energy. The spectrum can vary greatly with the rotor geometry and operational conditions because the aerodynamic flowfield is affected by these parameters.

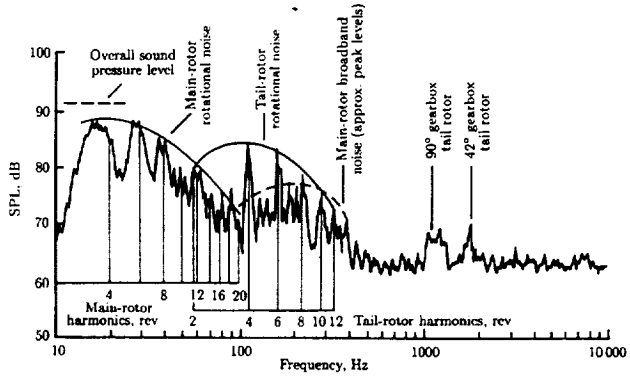

Figure 1.2 The frequency spectrum of a typical helicopter far-field noise signal (ref. 2).

1.1.3 Thickness effects– An aerodynamic disturbance (monopole) is created when a rotor blade passes through and displaces the air. This is often referred to as thickness noise, since its magnitude is dependent on the thickness of the rotor blade. The aerodynamic disturbances due to blade thickness generally propagate in the plane of the rotor and in this study the effects were seen at the microphones only when the rotor blade passed closest to them. (That is, the maximum sound pressure due to thickness effects recorded by a microphone occurred in phase with the blade passage over the microphone.) In this report, the calculated near-field pressure changes due to these aerodynamic disturbances are often referred to as thickness effects, and will be discussed in more detail in section 4.3.

1.1.4 High speed impulsive noise– When a rotor blade travels fast enough, shock waves can occur on the blade tips, which creates high speed impulsive (HSI) noise. HSI noise is the abrupt sound generated by highly localized aerodynamic events (quadrapole) on the rotor blade caused by the shock waves and therefore is also related to the thickness of the blade. HSI noise is generally associated with large, sharp, negative pressure peaks in

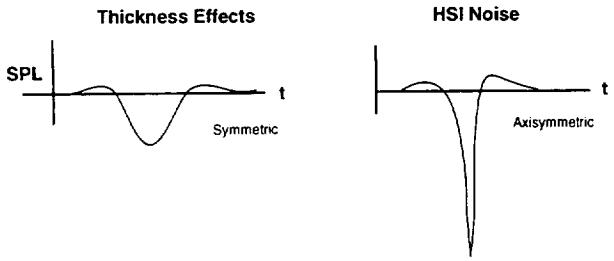

Figure 1.3 Schematic comparing general amplitude and wave shapes for thickness effects and HSI noise.

the time history and tends to propagate in the plane of the rotor (ref. 3). Figure 1.3 is a theoretical plot of sound pressure level (SPL) versus time. This figure compares the basic amplitude and wave shape of thickness effects and HSI noise.

HSI noise is generally an issue for "older" helicopters, such as the two-bladed Bell Huey UH-1H, used since the 1960s. (A two-bladed rotor typically has to operate with a higher tip Mach number than helicopters with more blades.) The Huey was designed before engineers fully understood the role of shock waves in noise generation. Significant progress has been made to reduce HSI noise by designing rotors that have thinner airfoils at the blade tip, and rotors that can operate at lower tip Mach numbers. Blade tip sweep is also used to reduce the effective tip Mach number to alleviate HSI noise, such as on the S-76 rotor (ref. 4).

1.2.5 BVI noise– BVI noise is a very high amplitude impulsive sound, usually dominating other rotorcraft noise when it occurs. When a helicopter operates in certain low speed, descent flight conditions, the upwash tends to convect the rotor wake (and the trailed blade tip vortices) into and above the rotor disk plane. Over certain parts of the disk the blades can pass close to the trailed tip vortex causing strong BVIs. The rapid variation in induced velocity associated with the tip vortex causes large, time varying fluctuations in loading on the leading edge region of the blade (dipoles), which generates the impulsive sound. Figure 1.4 illustrates how descending flight conditions generally create BVI.

Unlike HSI noise, which is known to propagate mostly in the plane of the rotor, BVI noise propagates out-of-plane, usually forward and down at about a 30 to 40 deg angle (ref. 3). This makes the noise more audible to an observer on the ground as a helicopter approaches to land. BVI conditions can also occur with tandem rotors, where under certain flight conditions, the tip vortices trailed from the front rotor can interact with the blades of the aft rotor (ref. 3).

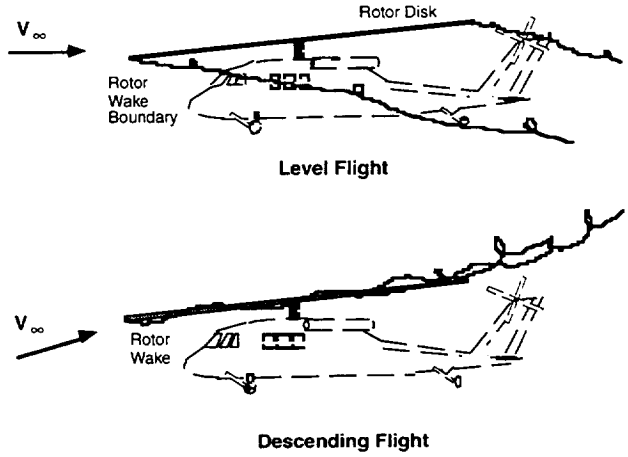

Figure 1.4 Flightpath effects on BVI noise.

A rotor blade can intersect a trailing vortex at different angles (from the vortex being perpendicular to the blade to nearly parallel), depending on the blade's azimuth position and the vortex age. The most prominent BVI event is one where the trailing vortex is nearly parallel to the blade, usually occurring near azimuth angles of 70 to 80 deg. Parallel BVI is known to be the strongest and most important event for acoustics because of the brief and dramatic changes the blade experiences along its entire span as it travels through the vortex flowfield (ref. 5). Figure 1.5 is a schematic of a parallel BVI. The helicopter is in forward flight (the rotor turning counter-clockwise as viewed from above) and the preceding blade has generated a tip vortex that a following blade will intersect.

BVI can be identified in the time history of an acoustic pressure trace by sharp positive or negative pressure pulses, depending on the rotational sense of the vortex. When a blade approaches (in a parallel manner) a clockwise-rotating vortex, the vortex first induces a negative angle of attack on the blade, followed shortly after by a positive angle. The top left of figure 1.6 is a schematic of a clockwise vortex and the approaching blade. The first plot illustrates the change in angle of attack the blade experiences as a result of the interaction with the vortex. This affects the lift on the blade, shown in the middle plot. The time rate of change of lift is related to the pressure propagated to an observer, as qualitatively shown in the lower plot. The figure and plots on the left (clockwise vortex rotation) are typical of advancing side BVI, where as the right hand figure and plots (counter-clockwise vortex rotation) are typical of retreating side BVI. The lower of these plots characterize typical BVI noise time histories.

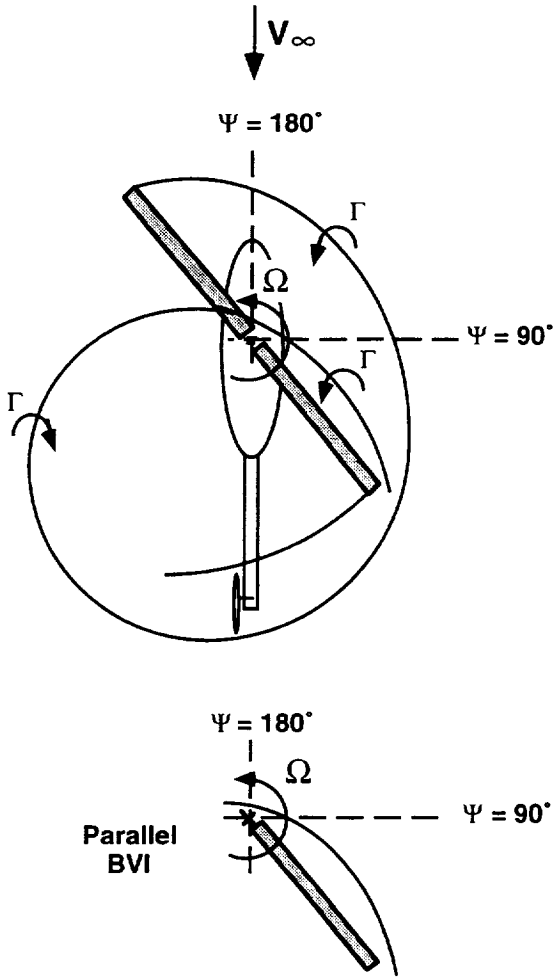

Figure 1.5 Schematic of parallel BVI on a helicopter.

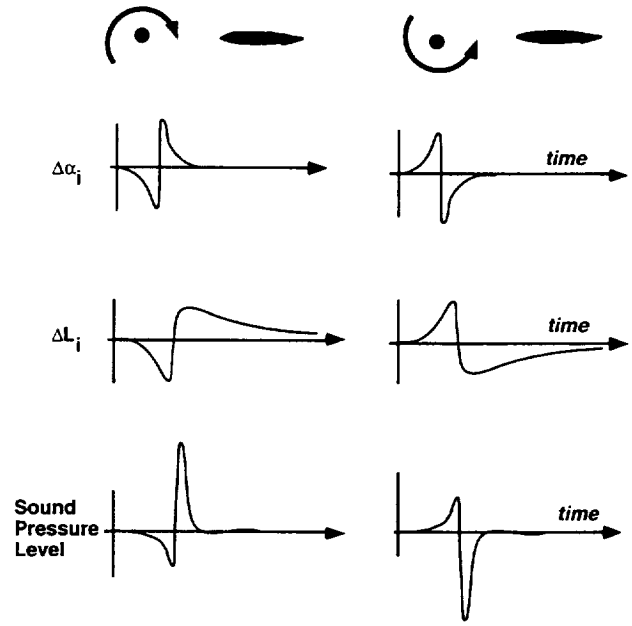

Figure 1.6. Example of the source of BVI noise.

The strength and acoustical importance of a typical BVI is governed by several parameters, such as; 1) local strength of the tip vortex, 2) induced velocity field and core size of the tip vortex, 3) local interaction angle between the blade and the axis of the vortex, 4) vertical separation distance between the vortex and the blade, and 5) local Mach number at the interaction (ref. 3).

1.2 Previous Work in BVI Acoustics

There has been extensive research, both experimental and computational, in the area of rotorcraft acoustics. The complexity of rotor aerodynamics and aeroacoustics have made isolating and modeling the BVI problem a challenging endeavor. One of the most difficult tasks in rotorcraft acoustics is to measure the radiated noise under carefully controlled conditions. Since the problem is intrinsically linked to the rotor wake, it is generally acknowledged that more detailed information on the trajectory and structure of the trailed tip vortices is also required before accurate predictions of BVI noise can be made.

1.2.1 Previous experimental BVI studies– The study of BVI noise began with the work of Leverton and Taylor (ref. 6) when community annoyance and aircraft detection started to become a concern. Since then, efforts to understand BVI experimentally have been made through flight testing, full- and model-scale wind tunnel testing, and tests using a "free vortex," which will be described below.

One example of flight testing done specifically to study BVI noise were the investigations performed by Schmitz and Boxwell (refs. 7 and 8). These authors obtained noise measurements generated by a Bell UH-1H in BVI flight conditions by flying in formation with a "quiet" aircraft designed specifically as an acoustic acquisition platform. The investigation studied the scalability of small-scale BVI to full-scale wind tunnel data, and the differences in BVI noise due to different main rotor blade sets. The studies showed the feasibility of scaling BVI noise (for advance ratios less than 0.2), and that blade tip modifications had only a slight attenuation of BVI noise (ref. 3).

One example of a full-scale wind-tunnel test specifically designed to study BVI was that of Signor et al. (ref. 9). Acoustic measurements generated by a full-scale BO 105 helicopter were acquired in the National Full Scale Aerodynamics Complex (NFAC) at Ames Research Center (ARC). These investigations compared BVI noise acquired in the wind tunnel to data taken in-flight, and also to model-scale rotor tests. This study found significant differences in BVI characteristics when comparing flight, full- and model-scale tests and concluded the differences were due to the difficulty in repeating the exact environment in which BVIs occur (ref. 9).

An extensive study was performed of a 1/7-scale main rotor of a Bell AH-1 helicopter in the anechoic Deutsch-Niederlaendischer WindKanal (DNW) (refs. 10 and 11). These tests involved simultaneous acquisition of blade-surface pressures and far-field acoustic data at a large number of microphone locations, and for a wide range of flight conditions. This test was extremely useful in determining BVI noise source locations on the rotor, and also the directivity from the rotor. More recent DNW tests have included flow visualization and laser-Doppler velocimetry in order to closely observe the rotor wake (ref. 12).

All of these studies were helpful in understanding BVI noise, but are still too complex to simulate by means of computational fluid dynamics (CFD). The DNW test began to provide a database for computations to compare with blade-surface pressures, but the details of the BVI event were still unknown. For example, a BVI event could be carefully observed with blade-surface pressure data and its propagation examined through microphone data, but this still does not provide enough information on the vortex strength, structure, and proximity to the blade. This kind of information can only be obtained under more controlled conditions using a simpler experimental setup.

McCormack and Surendraiah (ref. 13) were the first to examine BVI in a simulated rotary-wing environment where the rotor interacted with, but did not generate, the vortex in question. The rotor was operated with zero lift, so that it did not generate any notable tip vortices of its own. The vortex (to create a BVI) was generated by a semi-span wing mounted upstream of the model rotor. The generation of this independent and steady tip vortex from the wing enabled accurate control and measurement of the vortex strength and structure. The angle of attack of the wing dictated the strength and sense of rotation of the vortex. This independent wing also allowed the proximity of the vortex with respect to the blade to be controlled by adjusting the position of the wing in the wind tunnel. Placing this tip vortex in line with the quarter-chord of the rotor blades at the 180 deg azimuth, provided a parallel interaction. In addition, the wing tip could be extended or retracted to place the tip vortex above or below the plane of the rotor.

This independently generated vortex (completely separate from the rotor) is sometimes referred to as a "free vortex." The free vortex provides known parameters for the BVI, significantly reducing the complexity of the interaction, and enables the more detailed study of the individual parameters affecting the loads and resulting acoustics. The free vortex method was extensively applied in experiments by Horner (ref. 14) and Caradonna et al. (refs. 5, 15, and 16). These tests provided specific BVI statistics and rotor blade-surface pressure data that have been used for CFD code comparison and validation. The wind tunnel in these experiments was not acoustically treated, so off-surface pressure data could not be acquired.

In 1993, for the first time, a free vortex was used in conjunction with the acquisition of acoustic measurements as well as surface pressure data. The test described in reference 17, was designed by Kitaplioglu and Caradonna, and performed in the ARC 80- by 120-Foot Subsonic Wind Tunnel (refs. 17 and 18). A model rotor, 7.125 ft in diameter, was tested in this large, acoustically treated facility to reduce the influence of wall reflections or flow turbulence. The blades were rigid, symmetric, untapered, untwisted, and instrumented with 60 pressure transducers. There were 7 microphones in the test section, two in the near-field specially for CFD validation, and 5 in the far-field.

This test helped to eliminate several of the complexities and unknowns for a typical BVI, and provided an opportunity to compare acoustics data with CFD codes under much more controlled conditions. The processing of the near-field microphone data, the analysis of the data, and comparison with CFD results, are the primary goals of this report.

1.2.2 Previous computational BVI studies– The first step to predicting BVI noise is to calculate the unsteady aerodynamics on the blade surface, since it is the aerodynamic interactions on the rotor blade that generate noise. Widnall (ref. 19) performed some of the earliest theoretical studies of BVI noise in the 1970s, by computing the blade lift distribution during a typical BVI. The unsteady lift on the blade was calculated using a linear unsteady aerodynamic theory, with an oblique gust model of the acoustic disturbance.

Other numerical methods applied to helicopter aerodynamics and acoustics problems include lifting line, lifting surface, and panel methods (refs. 20–23). Nonlinear finite-difference models were later developed to more closely simulate the nonlinear, transonic flowfields

associated with an advancing blade. Examples are the Transonic Small Disturbance (TSD) equation (ref. 24), full-potential equation (ref. 25), Euler equations (ref. 26), and Navier–Stokes equations (ref. 27).

In the 1980s, a popular approach for predicting far-field acoustics was to take experimentally measured surface pressure data and apply Lighthill's acoustic analogy (ref. 28), which was put into a form known as the Ffowcs Williams-Hawkings equation (ref. 29). (In brief, Lighthill's acoustic analogy uses linear monopole and dipole terms, and nonlinear quadrople terms to model the combination of rotational, thickness, HSI, and BVI noise.) WOPWOP (ref. 30) is a code that was developed based on Farassat's advanced subsonic time domain formulation (ref. 31) the Ffowcs Williams-Hawkings equation. This code modeled the helicopter rotor acoustics relatively accurately, but required detailed blade-surface pressures and blade motion as input. That is, if detailed experimentally measured blade-surface pressures were used as input, the predicted acoustics was relatively accurate, but if predicted-surface pressures were used, the calculated results did not fare as well.

A Full Potential Rotor (FPR) analysis has been coupled with a code called Rotor Acoustic Prediction Program (RAPP) to predict rotor acoustics (ref. 32). First, from known flight information, FPR predicts the blade-surface pressures, and this is used as input to RAPP to predict the far-field acoustics. RAPP is not able to predict near-field acoustics because it treats the noise source as a compact source and neglects thickness effects and a near-field term in the mathematical model.

Another approach is the Kirchhoff method (ref. 33) which uses an imaginary surface off of the blade. This Kirchhoff surface requires the pressure and time derivatives on and normal to the surface. There has been limited success to date since the method requires accurate input of data off of the blade. However, in general, if the Kirchhoff surface is placed outside the region of nonlinearities, it will accurately predict the propagation of the sound (ref. 33).

In the late 1980s, Baeder pioneered the application of CFD to simultaneously compute the aerodynamics and acoustics of a 2-dimensional (2-D), nonrotating airfoil interacting with a parallel vortex (ref. 34). This work used the concept of the vortex-fitting method originated by Srinivasan (ref. 35) to the Euler/Navier–Stokes codes to calculate the aerodynamics of the unsteady interaction of a rotor with a vortex.

Srinivasan then wrote the Transonic Unsteady Rotor Navier–Stokes (TURNS) code (refs. 36–38) which is a direct CFD approach that can include prescribed vortices. The computational model calculates the density, three components of momentum, and energy at each grid point for each time step, and the grid rotates with the rotor blade. From the equation of state, the pressure can also be calculated at each point at each time. (See App. A for more details.)

Baeder and Srinivasan (ref. 39) used a version of the TURNS code, called TURNS-BVI (ref. 37), to compare calculated surface pressure data to the recent Caradonna BVI experiment described previously (ref. 15). A few cases were calculated at arbitrary near-field locations to examine the qualitative results of acoustic predictions. Good comparisons of the surface pressures were obtained (ref. 37), and the feasibility of using purely CFD in BVI computations and predicting the near-field acoustics was shown (refs. 38 and 39). In the current study, TURNS-BVI was used to calculate the acoustics at the same microphone locations and test conditions as in the wind-tunnel experiment (ref. 18), from which comparisons are made.

1.3 Motivation and Objectives

The Kitaplioglu-Caradonna wind tunnel experiment used in this study was specifically designed for comparison to numerical models. Certain parameters, too complex or costly for CFD to calculate, were measured and are known in this experiment. It is also the first time acoustics data has been acquired in this type of controlled environment.

The objectives of the study were several:

1. The experimental measurements of the near-field acoustics needed to be processed and analyzed to better understand the initial propagation of the acoustics of isolated BVI, and also to be compared to computational models.

2. An Euler/Navier–Stokes code was used to simulate the experiment for several test cases to examine the validity of the code. The validation could allow the CFD method to be used as a tool to better understand the complex BVI phenomena.

3. Several parameters that influence the CFD simulation, such as time accuracy and vortex strength, needed to be examined in order to obtain better quantitative comparisons.

4. The results from the CFD method form a numerical database that can be used to test several hypotheses, such as the effect of thickness or the directionality of BVI noise. This should reveal the suitability of the CFD results to test simpler, more efficient methods for BVI predictions.

5. One of the objectives of the wind tunnel experiment was to compare the experimental data with theory. This satisfied, it is hoped that this study will help researchers define future BVI experiments that could further validate the computational models. Also, a good comparison with theoretical models can give greater confidence to the experimentalists that the test results accurately measured the phenomena.

1.4 Organization

The organization of the technical memorandum begins with a description of the experiment, and the experimental data acquisition and processing in section 2. The computational code is briefly described along with some specifics relevant to the present work in section 3. Section 4 is a presentation and discussion of all the results in the study. This includes the experimental results, a comparison of CFD results with experiment, and the effect of time accuracy, thickness effects and microphone position. Finally, summary and conclusions are presented in section 5.

2 The Experiment

This section describes the model-scale helicopter rotor experiment which studied parallel BVI and was performed at the ARC 80- by 120-Foot Subsonic Wind Tunnel in 1992. The experimental set-up and associated hardware is described. The acoustics data was acquired, processed, and analyzed using the ALDAS software program, described in section 2.2.1, and will be explained through an example case. Experimental results are presented for eight different test conditions along with a discussion of general trends and noted deviations. It is important to recall that this test took the approach of performing an experiment that closely resembles the simplified conditions that would be more amenable to analysis with CFD methods.

2.1 Experimental Set-up

The objective of the experiment was to simulate the aerodynamics and acoustics of parallel, BVI. Independent control of the interaction parameters (such as vortex sense and location) helped to refine the test for comparison with CFD methods. The experiment was a wind-tunnel test (where flow conditions could be closely monitored), with a model rotor, (which had a simple geometry and was aeroelastically stiff), and had an independently generated vortex upstream of the rotor (providing a known vortex strength and location). The rotor was operated at nominal thrust, so that the influence of its own self-generated wake would be minimized. Figure 2.1 shows a schematic of the experimental set-up. This figure illustrates how the blade-vortex separation distance and the vortex sense of rotation were independently controlled by the height and angle of the vortex generator.

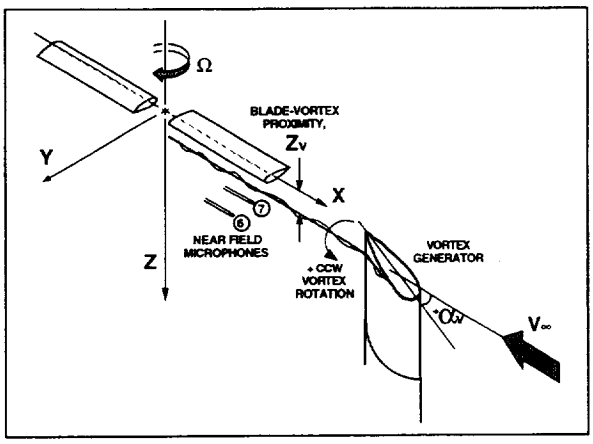

Figure 2.1 Schematic of experimental set-up in wind-tunnel test section.

2.1.1 Facilities– The ARC 80- by 120-Foot Subsonic Wind Tunnel is part of the NFAC located at Moffett Field, California. This large facility allowed the small-scale experiment to be minimally affected by wall reflections or flow turbulence. The wind tunnel is acoustically treated with 6 in. of foam on the walls and ceiling and 10 in. on the floor. The maximum velocity in the test section is 100 knots, and the axial turbulence intensity is less than 0.5 percent (ref. 40). Figure 2.2 is a photograph of the hardware in the test section. In this photo the airflow travels from left to right, flowing past the vertical wing and then the rotor.

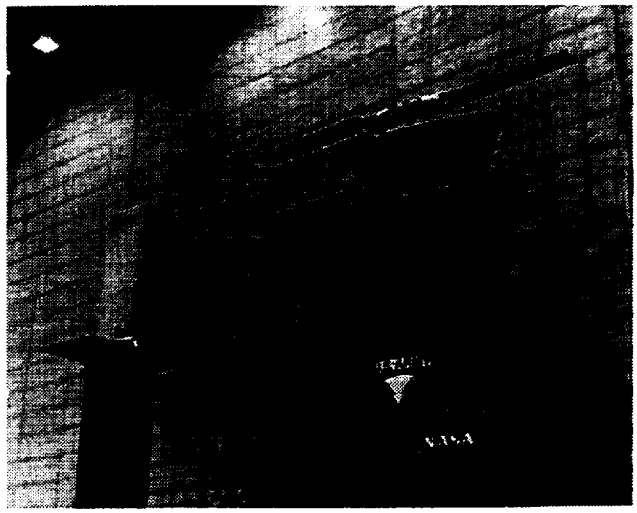

Figure 2.2 Photograph of BVI experiment in the ARC 80-by 120-Foot Subsonic Wind Tunnel.

2.1.2 Rotor geometry– The two-bladed, teetering rotor had a diameter of 7.125 ft. The blades were untwisted with a rectangular planform with a constant 6-in. chord, comprised of the NACA 0012 airfoil section. The hover tip Reynolds number was approximately one million for an advance ratio of 0.2. One blade had 30 absolute pressure transducers on the top surface, while the opposite blade had 30 transducers on the lower surface, distributed at three spanwise positions. The blades were constructed of balsa wood and carbon/epoxy composite, and were very stiff in bending and torsion to minimize aeroelastic effects. Full cyclic pitch and collective pitch control were provided through a swashplate. In forward flight, the rotor was trimmed to minimum flapping, and operated at zero thrust to minimize self-generated tip vortices. The rotor rotated clockwise as viewed from above.

2.1.3 Vortex generator– A streamwise vortex was generated directly upstream of the rotor with a 18-in. chord, semi-span wing of NACA 0015 airfoil section. The wing was mounted vertically in the wind tunnel and could extend or retract vertically to place the streamwise vortex above or below the rotor plane. The Reynolds number for the vortex generator wing was approximately 600,000. The tip vortex strength and structure were not directly measured in this experiment. However, in a previous experiment McAlister and Takahashi performed extensive measurements of the trailed vortex from the NACA 0015 wing (ref. 41). The strength and structure of the vortex in the BVI test is assumed to be consistent with the McAlister and Takahashi data. Figure 2.1, shown previously, illustrates the blade-vortex vertical separation distance, Z_V, and the vortex generator angle of attack, α_V.

It is noted that the vortex generator chord is three times larger than that of the rotor. Caradonna et al. (ref. 14). found the rotor blade pressure variation to be insensitive to vortex core size for the miss distances used in this study (±0.25 rotor chords). Caradonna stated that the structure of the trailing vortex from the fixed wing was essentially the same as that from a rotor, therefore, the wing-generated tip vortex has good utility for this investigation.

2.1.4 Microphones– There were seven, 1/2-in. diameter, Bruel and Kjaer microphones located in the test section: two in the near-field and five in the far-field. Only the near-field microphones, designated numbers 6 and 7, are considered in this study. The microphones were calibrated every day and were consistently within ±0.1 decibels for the pistonphone signal of 124 dB, and ±1 Hertz for a 250 Hz signal.

Both near-field microphones were located 12 in. (2 rotor chords) below the rotor, at the 88 percent rotor radius with respect to a blade position at 180 deg azimuth angle. When the rotor was phased at the 180 deg azimuth (blades oriented streamwise), microphones 6 and 7 were 10.25 and 2.25 in. in front of the rotor quarter-chord, respectively. Figure 2.3 below shows the position of the near-field microphones relative to a rotor blade. Microphones 6 and 7 are at 49 and 80 deg down from the rotor plane, as measured from the rotor quarter-chord at 88 percent radius, when the rotor is at Ψ = 180 deg.

It should be noted that the rotor-blade quarter-chord passed closest to microphones 7 and 6 when the rotor was at 183 and 195 deg, respectively, as shown in figure 2.4.

2.1.5 Test cases– There were eight different test configurations chosen for examination in this report. There were two different hover Mach tip numbers (0.6 and 0.7), two different vortex generator angles (±12 deg),

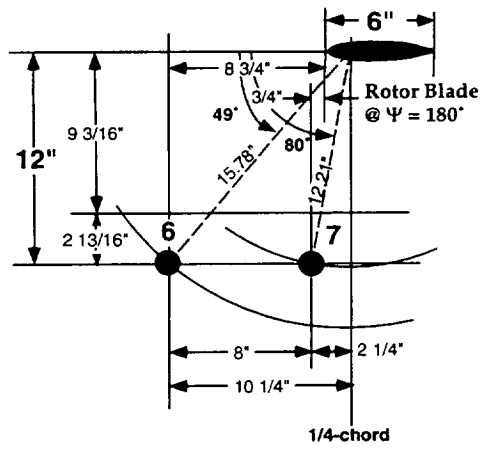

Figure 2.3 Position of microphones 6 and 7 with respect to rotor blade at 0.88R and 180 deg azimuth angle.

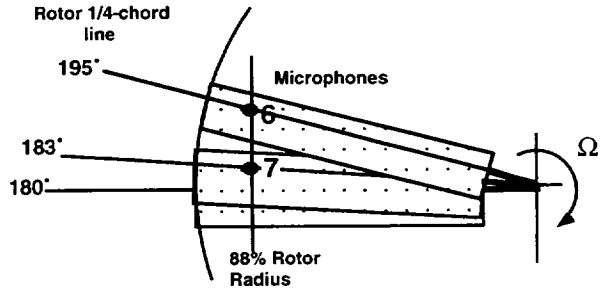

Figure 2.4 Schematic of rotor quarter-chord line passing over microphones.

and two different vortex locations (above and below by 0.25 rotor chords). Figure 2.5 illustrates the experiment as viewed from above and shows the vortex generator at the two different angles and shows a typical BVI occurring in parallel to the rotor quarter-chord.

There has been some discussion (C. Kitaplioglu, F. Caradonna, and Y. Yu, personal communications) that the interaction was actually parallel at the leading edge of the blade in some cases, not the quarter-chord, as is assumed by the CFD computations. This affects only the phasing (time) of the BVI noise event and not the strength and structure of the acoustic pressure time history.

Figure 2.6 is a schematic, looking downwind in the plane of the rotor, showing the four test cases studied at the two different hover tip Mach numbers of 0.6 and 0.7. The advance ratio was kept at 0.2 for each hover tip Mach number by adjusting the wind tunnel velocity. Figure 2.6 also illustrates the vortex sense and location. The horizontal arrow near the surface of the blade in each case

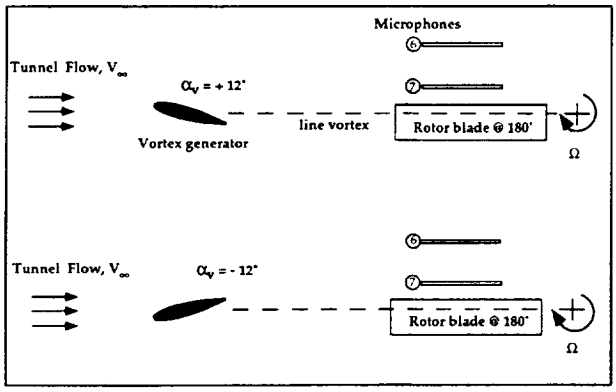

Figure 2.5 Schematic of test set-up (as viewed from above) showing parallel BVI occurring at the rotor quarter-chord.

indicates the induced horizontal velocity experienced by the blade as a result of the vortex encounter. The peak vertical induced velocities produced by the vortex, as the vortex passes by the rotor blade, are expected to be of equal and opposite magnitude because the rotor is a symmetrical airfoil section and non-lifting. Cases II and IV (clockwise vortex rotation) are typical of advancing side BVI, and Cases I and III (counter-clockwise rotation) are typical of retreating side BVI.

2.2 Acoustic Data Acquisition and Analysis

Three data acquisition systems were necessary in this experiment. The Standard Wind Tunnel System (SWTS) recorded wind tunnel and rotor parameters, and a 32-channel, 16-bit analog to digital (A/D) conversion system acquired data from the 60 pressure transducers. Acoustic Laboratory Data Acquisition System (ALDAS), a Macintosh based acoustic data system, recorded the microphone data (refs. 42 and 43). ALDAS, and the acquisition, reduction, and analysis process, as performed by the author, are described later.

2.2.1 ALDAS– The ALDAS (ref. 42) was used for acoustic data acquisition and reduction. Experimental acoustic data were digitized at 1024 points per rotor revolution on a Macintosh-based, four-channel, 12-bit A/D data system. The microphones were calibrated daily using a pistonphone, and all incoming data were filtered at 10 KHz to prevent aliasing errors. Thirty rotor revolutions of data were acquired for each test condition. The results were time-averaged in a phase locked sense using the rotor one-per-revolution trigger signal, which resulted in a one-revolution long, ensemble averaged time history of the acoustic pressure.

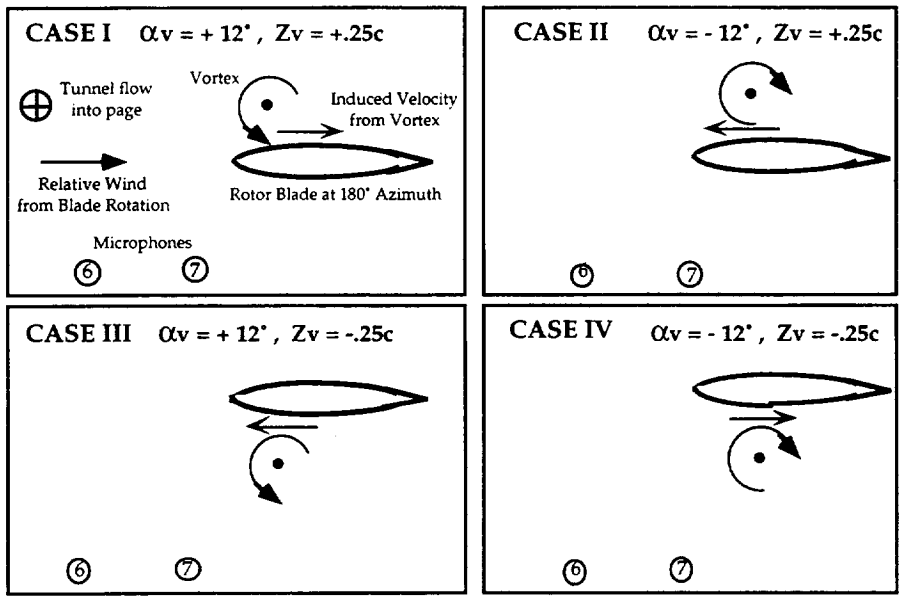

Figure 2.6 Schematic illustrating four BVI geometries examined at two different hover tip Mach numbers.

In addition, the experimental data underwent a thorough review to check for high background noise, corruption due to electrical interference, "self noise" (noise due to airflow over the microphone or other hardware), and for repeatability. The data presented in this report was found to be acceptable in all of the above criteria.

2.2.2 Example of averaging procedure– The data were saved as a single time history, 30 revolutions long, in units of Counts versus Data Points. (A 12-bit A/D data system means that the integer value of Counts will vary from 0 to $2^{12} - 1 = 4096$.) The test data of Case I, microphone 6 at $M_{tip} = 0.6$ (Run 49, Test Point 09), will be used throughout this section as an example of how the averaging procedure was performed.

Figure 2.7 is a plot of several revolutions of raw data acquired for the example case. The sharp BVI peaks and relatively low noise between events are the result of the closely controlled test environment, and is typical of data recorded throughout the test. Note that there is still a variation in the peak to peak values and a high frequency noise between separate BVI events. Figure 2.8 is a corresponding frequency spectrum of the unaveraged data. This spectrum, although less detailed, is similar to the frequency spectrum shown in figure 1.2, and shows the harmonic "humps" typical of those found in helicopter noise signatures.

Figure 2.9 shows a single revolution of unaveraged data. Again, even the raw data is "clean" with few other noise sources contaminating the BVI signature. Figure 2.10 shows the result of ensemble averaging over 30 cycles. Note that in the averaged case, the high frequency "noise" between the BVI events is eliminated, and there is a slight decrease in the maximum and minimum peak values.

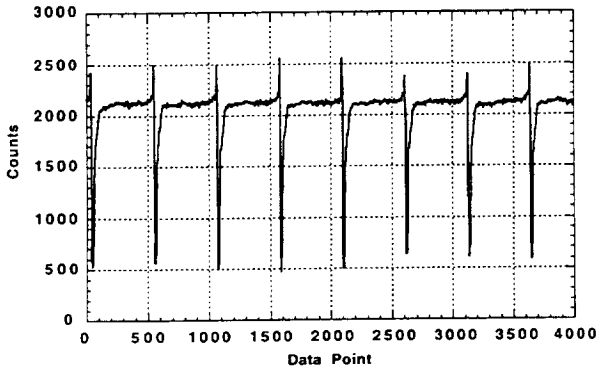

Figure 2.7 Example of unaveraged experimental data in original units. Case I, $M_{tip} = 0.6$, microphone 6.

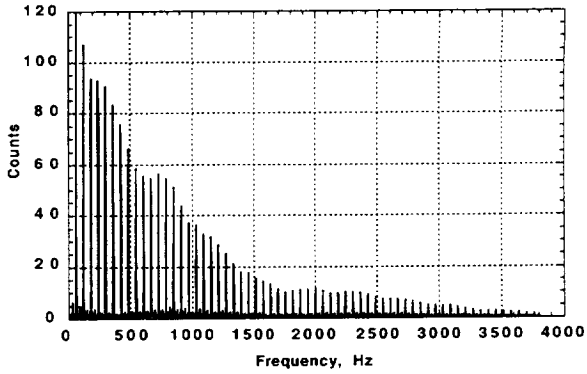

Figure 2.8 Frequency spectrum of 30 revolutions of experimental data. Case I, $M_{tip} = 0.6$, microphone 6.

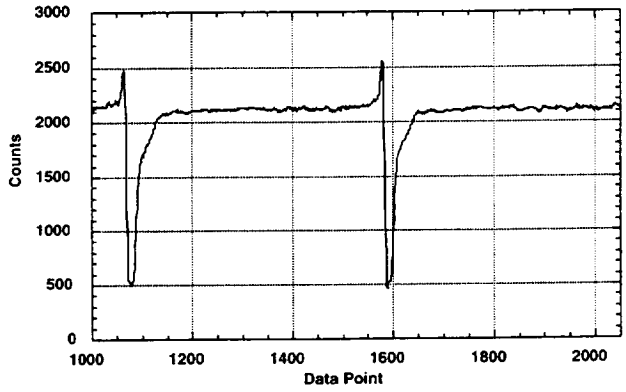

Figure 2.9 Example of a single revolution of pressure data, unaveraged in original units. Case I, $M_{tip} = 0.6$, microphone 6.

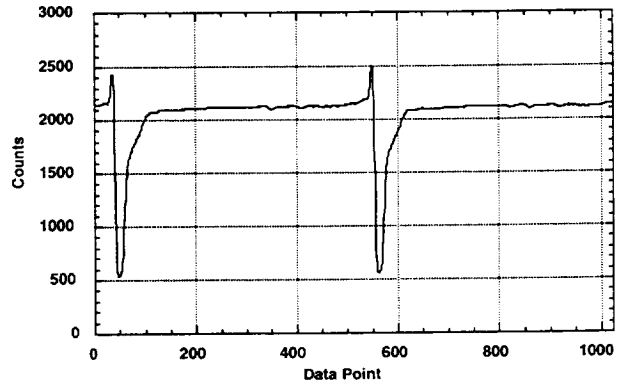

Figure 2.10 Example of one revolution of averaged pressure data. Case I, $M_{tip} = 0.6$, microphone 6.

Figure 2.11 shows an example of the averaging statistics calculated for each test case. The first (top) plot shows the maximum deviation from the average signal in percent, which is nearly ±20 percent in this example. The second plot shows the standard deviation from the average signal in percent, and is less than 10 percent. In the third plot, the cycles with the maximum and minimum peak-to-peak values are plotted together, along with the average, and the pooled standard deviation is less than 5 percent. In this example, cycle 16 of 30 had the maximum peak to peak value, and cycle 22 had the minimum. Any sample with a standard deviation greater than 10 percent could be clearly identified in the averaging statistics and was considered an unacceptable data sample.

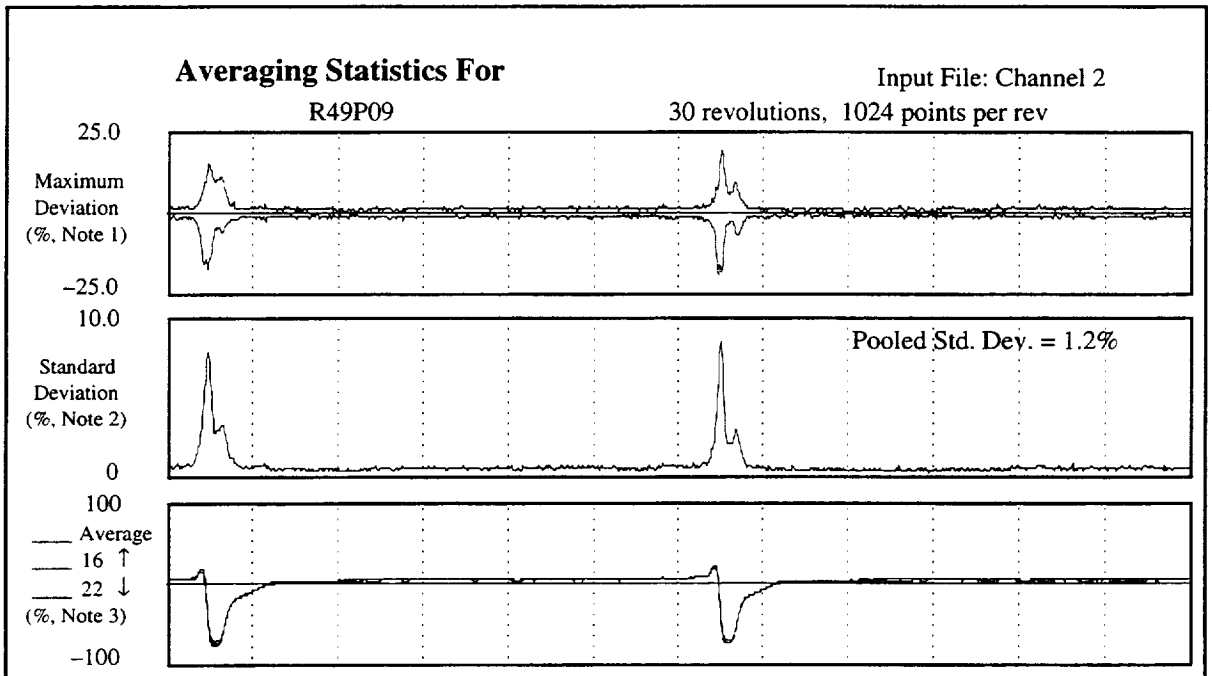

Point	Average Value	Standard Deviation	Maximum Pos. Delta	Maximum Pos. Cycle	Maximum Neg. Delta	Maximum Neg. Cycle
1	2142	15.01	31	23	28	17
2	2141	16.02	27	23	31	18
3	2140	17.01	30	23	35	27
4	2143	13.75	38	1	36	27
5	2146	13.66	40	1	27	27
6	2146	11.95	29	1	20	20
7	2146	10.63	21	1	16	27
8	2147	10.97	21	1	20	27
9	2146	15.55	27	1	38	2
10	2147	15.69	26	1	38	6

Peak to Peak in Counts: 1965 Peak to Peak in Pascals: 106.4845

Note 1. Maximum deviation from average signal as a percent of averaged peak to peak.
Note 2. Standard deviation from average signal as a percent of averaged peak to peak.
Note 3. Time histories as a percent of averaged peak to peak plotted around average mean.

Figure 2.11 Averaging Statistics for Run 49, Point 09, Case I, M_{tip} = 0.6, microphone 6.

Note that ensemble averaging is always necessary to get a clean, mean representative cycle of the data, but a slight reduction in the peak-to-peak values is an unfortunate result. This is different from CFD predictions, which do not require any averaging procedure, and perhaps explains some of the overpredictions shown later in the results.

The measured data was converted to SPL in Pascals versus blade azimuth angle in degrees. The pistonphone calibration signal determined the relation of voltage to Pascals. The pistonphone provided a known SPL, and the microphone recorded a certain voltage. The voltage is digitized as Counts and converted to Pascals.

Some test cases were run twice on different days to examine experimental repeatablility. Figure 2.12 illustrates the typical variation on different days, after performing the data acquisition and averaging procedure. The most recent cases (larger run numbers) were chosen to represent the test conditions used in this study.

The experimental uncertainties were estimated to be ±4 deg in azimuth angle, due to 1/rev trigger inconsistencies and uncertainty of the exact location of the line vortex with respect to the rotor quarter-chord (C. Kitaplioglu, F. Caradonna, and Y. Yu, personal communications). Amplitude error is estimated to be ±5 percent of the peak-to-peak value due to typical variability seen in the peak-to-peak amplitudes in the raw data and the effects of the averaging procedure.

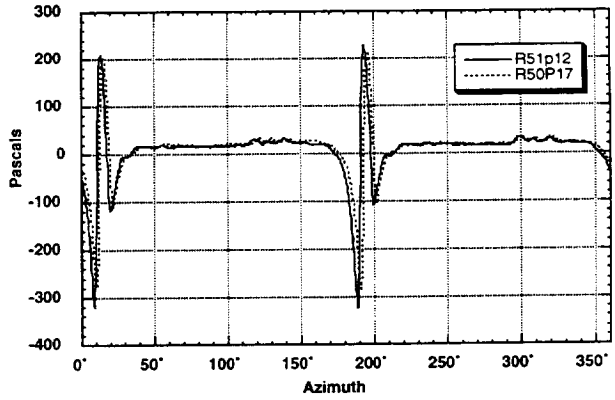

Figure 2.12 Example of two final plots of the same conditions tested on different days. Case II, M_{tip} = 0.6, microphone 6.

3 Computational Issues

The accurate numerical simulation of the helicopter rotor flowfield continues to be one of the most challenging problems in applied aerodynamics. Improved numerical algorithms have enabled advances in CFD to solve these complex fluid motion problems. An Euler/Navier–Stokes computational model has been used to simulate the previously described experiment (ref. 44). A detailed description of the governing equations and numerical algorithm is provided in Appendix A. This section does not describe the code, but briefly discusses some computational issues relevant to the present study.

First, the Euler equations, which assume inviscid flow, are briefly discussed. Second, the computational grid used in this study is described. Third, the treatment of the vortex and the Scully Vortex model is described. Finally, the effect of time accuracy and a brief description of Newton sub-iterations used by the code are discussed.

3.1 Governing Equations

A parallel BVI experiment was simulated using the TURNS CFD code, which can be used in either Navier–Stokes or Euler mode. The choice of governing equations affects the computational time and the level of physics modeled. In this study, it is assumed that the BVI do not result in flow separation so viscous effects are minimal and the Euler equations are able to capture most of the important features of the flow. The Euler equations are preferable to the Navier–Stokes equations due to their lesser computational overhead, yet the Euler equations are still able to model the convection of vorticity and nonlinear compressibility effects that can accompany BVIs. Thus, all of the computed solutions to the present study were run in Euler mode, which neglects any viscous terms. Furthermore, the Euler equations are a superset of the acoustic wave equation, and are able to accurately model nonlinear wave propagation away from the rotor blade surface.

3.2 Computational Grid

Computational grids for calculating the aerodynamics of rotor blades have tended to be highly clustered in the vicinity of the rotor-blade surface, with a coarse distribution of points away from the blade (ref. 39). In this study, a finer grid is used away from the rotor-blade surface to more accurately calculate the near-field acoustics, as well as the aerodynamics. Noise tends to propagate outward in a spherical pattern, and the grid was refined in the direction normal to the blade to maintain finer spacing for several chord lengths away from the blade surface. The three-dimensional (3-D) grid was constructed from a series of two-dimensional (2-D) hyperbolic C-grids (ref. 39). Each spanwise section was curved and spaced such that they remained at a constant radial distance from the rotational axis, and they were rotated in the azimuthal direction to maintain fine clustering near the linear characteristic curve (ref. 39). The flowfield was discretized using 169 points in the wrap-around direction with 121 points on the blade surface, 45 points in the spanwise direction with 23 points on the blade surface, and 57 points in the normal direction. This gave a total of over 430,000 grid points.

Figure 3.1 illustrates the grid in the plane of the rotor, and figure 3.2 illustrates the grid at a cross section of the blade at the 88 percent rotor radius. These grids are refined in the leading and trailing edges of the rotor blade in order to best capture the BVI acoustics.

The CFD analysis calculates the density, three components of momentum, and energy at each grid point for each time step. From the equation of state, the pressure can also be calculated at each point at each time. Since the grid rotates with the blade, and the microphones are stationary in the tunnel, the computed data must be interpolated at each time step for each "simulated" microphone location.

3.3 Vortex Management

The flowfield was initialized by computing the quasi-steady solution, without the line vortex, at a blade azimuth of 0 deg. Since the rotor was symmetrical and set to 0 deg

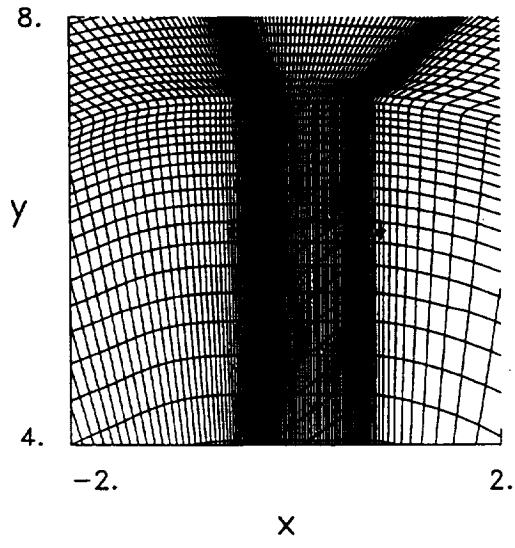

Figure 3.1 CFD grid in the plane of the rotor.

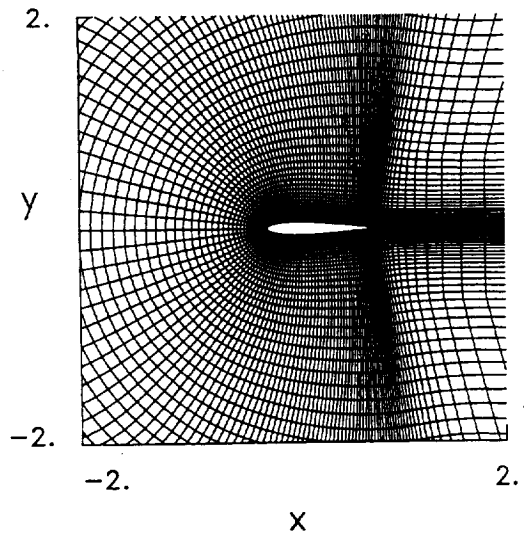

Figure 3.2 CFD grid at the 88 percent cross section of the rotor blade.

of collective with no cyclical or flapping motions, the computational time was reduced in half by applying symmetry to the boundary conditions, and therefore only calculating one-half of the flowfield. (The converged quasi-steady solutions were obtained in approximately 20 min of CPU time on a Cray Y-MP C90.) The initial unsteady computations (until a blade azimuth of 90 deg) were also computed without the line vortex, on one-half of the flowfield. At this point, the vortex was introduced into the flow and preserved using the vortex fitting method of Srinivasan (refs. 36 and 45). When introducing the vortex, the flowfield is no longer symmetric and the flowfield for the entire blade is now calculated. The convection of a line vortex in a free stream is a known solution of the Euler equations, and was added to the solution of the rotor blade without a line vortex. The combined nonlinear flowfield is also a solution of the nonlinear Euler equations, and so the solution of a convecting line vortex in the freestream was subtracted from the combined solution at every time step after the vortex was initialized. This nonlinear method reduced the numerical dissipation of the vortex and allowed for the adequate resolution of the vortex effects even where the grid was very coarse (ref. 46).

The line vortex was introduced when the advancing blade was at the 90 deg azimuth location and the solution was stopped when that blade reached the 270 deg. The vortex was treated as an infinite-line vortex that remained stationary as the blade rotated past it and the induced velocities in the axial and radial directions were neglected. (It is important to note that unlike the computational assumption that the vortex remained stationary as the blade passed by, experimental flow visualization showed otherwise and will be discussed in section 4.4.)

3.4 Vortex Model

The details of vortex-fitting into the TURNS code are described by Srinivasan in reference 37, and a brief description is presented here.

The Scully core model (ref. 47) for a rectilinear vortex was used to define the free vortex:

$$\frac{v_\theta}{U_\infty} = \frac{\hat{\Gamma}}{2\pi r}\left(\frac{r^2}{r^2 + a_0^2}\right) \tag{3.1}$$

where v_θ is the tangential velocity component, U_∞ is the freestream velocity, and r is the radial distance from the vortex center nondimensionalized by the chord of the rotor blade, c. The nondimensional core radius of the vortex, a_0, and the nondimensional vortex strength, $\hat{\Gamma}$, are defined by:

$$\hat{\Gamma} = \frac{\Gamma}{U_\infty C} \qquad a_0 = \frac{a}{c} \tag{3.2}$$

where C is the chord of the vortex generator, and c is the chord of the rotor blade. In addition, the radial momentum equation:

$$\frac{dp_v}{dr} = \frac{\rho_v v_\theta^2}{r} \tag{3.3}$$

and conservation of total enthalpy:

$$H_t = \frac{\gamma}{\gamma - 1}\left(\frac{p_v}{\rho_v}\right) + \frac{Q^2}{2} \tag{3.4}$$

were used to determine the pressure and density fields, where p, r, and g represent pressure, density and ratio of specific heats, respectively, H_t is total enthalpy, and $Q^2 = u^2 + v^2 + w^2$. The total energy of the convecting vortex is:

$$e_v = \frac{p_v}{\gamma - 1} + \frac{1}{2}\rho_v Q^2 \tag{3.5}$$

The calculations were performed using a nondimensional vortex strength of 0.406, unless otherwise stated, and a nondimensionalized viscous core radius of 0.17 for the vortex generator at ±12 deg angle of attack. These values were used by Caradonna et al. (refs. 5, 14, and 15) who

references personal communications with McAlister and Takahashi, who performed extensive measurements of the trailing vortex generated by a NACA 0015 wing. However, when McAlister and Takahashi presented their final report in 1991, they specified $\hat{\Gamma} = 0.35$ as the appropriate value for the NACA 0015 airfoil at ±12 deg angle of attack (ref. 41). All eight test cases in the computational study were calculated with $\hat{\Gamma} = 0.406$, but two of the cases were also calculated with $\hat{\Gamma} = 0.35$, and will be discussed in section 4.4.

3.5 Time Accuracy

Initial results of the computational model showed some oscillations in the time histories and inspired an investigation into whether increased time accuracy would eliminate the fluctuations. The effect of time accuracy was investigated by adjusting the number of Newton sub-iterations that the code performed. (Appendix A has a detailed description of the Newton sub-iteration procedure.) The basic scheme is only first order accurate in time without the Newton sub-iterations. Therefore, the sub-iterations are required to obtain the higher second order time accuracy, and as additional sub-iterations are performed, the solution becomes more accurate, to a point. More than 5 sub-iterations were found to have little effect. It was determined that five sub-iterations would be used at times closest to the BVI. If the residual for a given time step decreased by more than a factor of 50 during the Newton sub-iterations, then no further sub-iterations were performed at that time step. As a result, only three Newton sub-iterations were used during most of the calculations, except from 184 to 227 deg where the five sub-iterations were used.

3.6 Previous Validations

The development and validation of the Euler/Navier–Stokes CFD code began with examining blade-surface pressures for a rotor in hover. Srinivasan et al. (ref. 45) performed an initial study with a TURNS predecessor to examine the accuracy of the calculated blade-surface pressures for the steady case. Comparisons were made for a test conducted in an Army 7- by 10-Foot Subsonic Wind Tunnel experiment, and the computed results were found to match well (ref. 36). Figure 3.3, taken from reference 36, shows the comparison of experimental surface pressure data with the computed predictions. The next step in the development and validation of the code was to examine blade-surface pressures for a rotor in forward flight, and then for a rotor encountering a vortex in forward flight. Baeder et al. (ref. 38) examined the flow characteristics of a rotor encountering a vortex in forward flight, and calculated pressure both on and off the rotor blade surface. The blade-surface pressures matched well, and the near-field acoustics appeared qualitatively accurate (refs. 37 and 38). (Experimental acoustics data, that is, pressure data off the blade surface, was not available at that time.) Figure 3.4, taken from reference 38, is a comparison of surface pressures of a rotor blade encountering a vortex in forward flight.

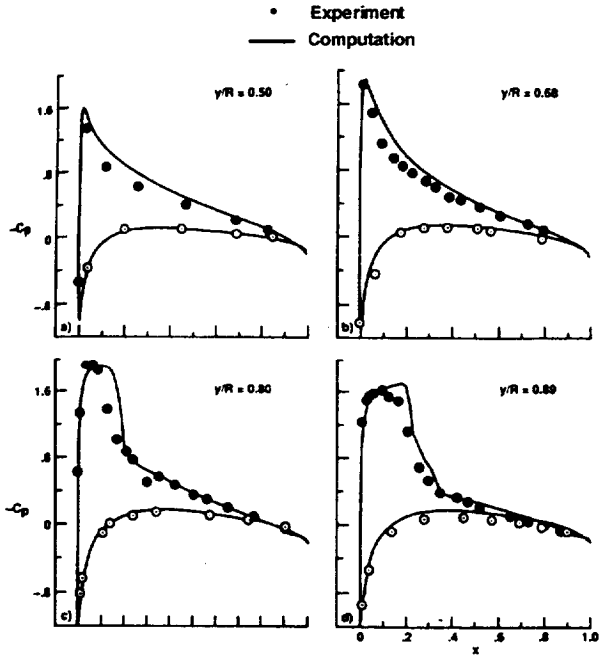

Figure 3.3 Comparison of experimental and computational blade-surface pressures for a rotor in hover (M_{tip} = 0.794, θ_c = 12 deg, and Re = 3.5 × 10^6) (ref. 36).

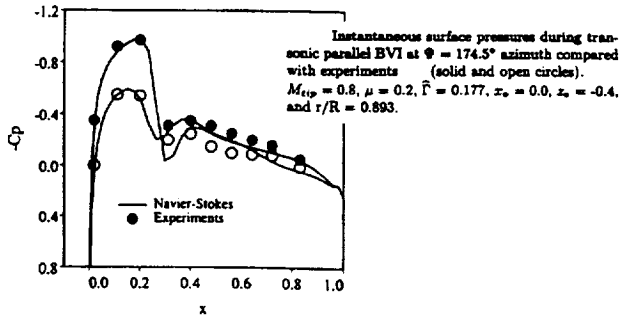

Figure 3.4 Comparison of experimental and computational blade-surface pressures for a rotor in forward flight (ref. 38).

4 Results and Discussion

An extensive array of test cases were measured in the experiment. Eight specific cases were chosen for the present study to examine the effects of positive and negative vortex rotation, the vortex passing above and below the rotor, and subsonic and transonic tip speeds. The experimental data for the eight test cases are presented along with a discussion of the trends and deviations. CFD calculations have been compared to the experimental data and are presented in section 4.2. Only four computed cases were needed for the CFD study, since the cases are symmetric and the data for the other four cases can be extracted at opposite points in the flowfield, above or below the rotor. Some additional CFD computations were performed to study the influence of aerodynamic thickness effects, vortex strength, Newton sub-iterations, and directionality of BVI radiated noise.

4.1 Experimental Data

The experimental data are presented as pressure time histories over 120 deg of rotor azimuth. Plotting the data in this manner (SPL in Pascals for Ψ = 120 deg to 240 deg) provides a detailed examination of the BVI event. Figure 4.1 presents the experimental acoustics data of the near-field microphones for the eight test cases examined in this study. The data in the top four plots were acquired at a hover tip Mach number of 0.6, and the lower four plots at a hover tip Mach number of 0.7. The tunnel velocity was adjusted in each case to maintain an advance ratio of 0.2. Each plot shows the pressures measured by microphones 6 and 7, which are represented by solid and dashed lines, respectively. The schematic in the lower left hand corner of each graph illustrates the vortex sense of rotation and location, and the locations of the microphones with respect to the rotor blade at the 180 deg azimuth angle for each case. The vortex rotated counter-clockwise (CCW) (representative of retreating blade BVI) for Cases I and III, and clockwise (CW) (representative of advancing blade BVI) in Cases II and IV. The rotor passed below the vortex in Cases I and II, and passed above the vortex in Cases III and IV. Note the expanded pressure scale for the M_{tip} = 0.7 cases.

Table 4.1 lists the sound pressure peak-to-peak amplitude for each test case. (The peak-to-peak amplitude is the absolute change in pressure between the maximum and minimum peaks in the time history.) Both microphones recorded significantly higher peak-to-peak amplitudes for the M_{tip} = 0.7 case. This is expected, and is caused by the increased Doppler and compressibility effects associated with the higher tip Mach number. The general trends (in the time history waveform), were found to be similar for both rotor tip Mach numbers.

Microphones 6 and 7 are the same distance below the rotor plane, but different distances from the rotor quarter-chord, as shown in figure 4.2. If it is assumed that the maximum sound radiates from the rotor quarter-chord when the rotor is at Ψ = 180 deg, and the speed of sound is 1087 ft/s, then the sound would arrive at microphone 7 about 3 deg of rotor azimuth earlier than microphone 6 for M_{tip} = 0.6, and about 3.5 deg earlier for M_{tip} = 0.7. This simple linear theory was used to determine the approximate time for the maximum pressure to arrive at the two locations for the two different hover tip Mach numbers, and are shown in table 4.2.

Again, the linear theory assumes the sound originates from the rotor quarter-chord when the rotor is at Ψ = 180 deg and that it propagates linearly and uniformly towards both microphones. Since the blade-vortex encounter was believed to sometimes occur at the leading edge and that some nonlinearities will exist in all cases examined, this information only provides "rough" figures with which to compare the experimental and computed data.

The plots of experimental data show that the initial pressure peak arrived at microphone 7 between Ψ = 185 and 190 deg for M_{tip} = 0.6, and between Ψ = 190 and 195 deg for M_{tip} = 0.7. The initial peaks for microphone 6 occurred consistently about 5 deg of azimuth later. This is expected and close to the rough figures calculated by linear theory.

The peak-to-peak sound pressure amplitude for microphone 7 for the CW cases are higher in amplitude than those for microphone 6. This is expected due to the different distances described previously. However, despite microphone 6 being farther away from the location of the BVI event, the peak-to-peak pressure values of microphone 6 are higher than those for microphone 7 for the CCW cases. This is possibly due to the direction in which the BVI sound waves propagate. The effects of directionality will be discussed in more detail in section 4.7.

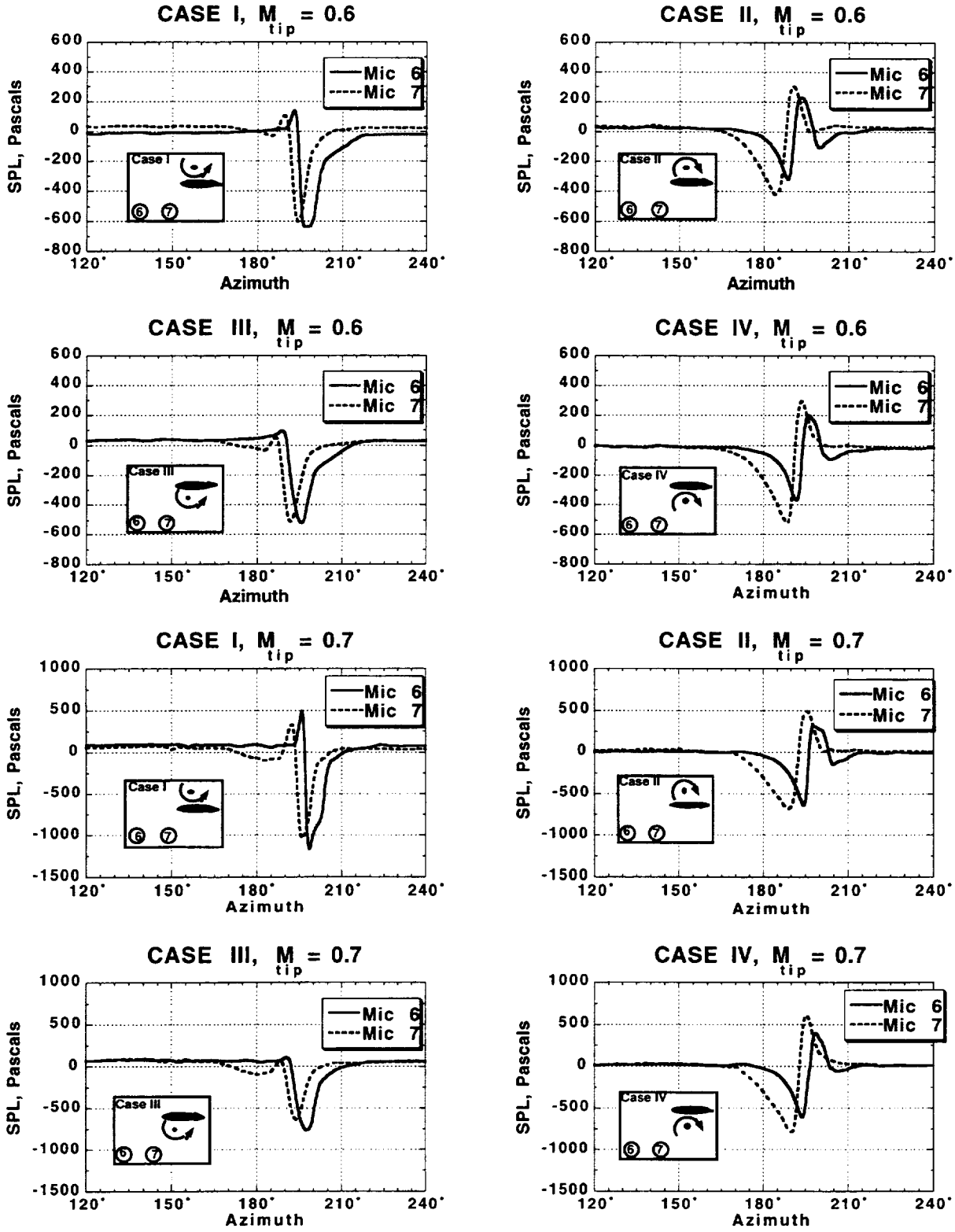

Figure 4.1 Experimental acoustic results for microphones 6 and 7 for eight BVI test conditions.

Table 4.1 Peak-to-peak pressure amplitude in Pascals for experimental data

	Test conditions			Peak-to-peak amplitude
$M_{tip} = 0.6$	Mic	α_v	Z_v	Experiment
Case I	6	12	0.25	786.12
Case II	6	12	–0.25	549.73
Case III	6	–12	0.25	634.35
Case IV	6	–12	–0.25	575.83
Case I	7	12	0.25	708.58
Case II	7	12	–0.25	722.66
Case III	7	–12	0.25	575.51
Case IV	7	–12	–0.25	825.94
$M_{tip} = 0.7$	Mic	α_v	Z_v	Experiment
Case I	6	12	0.25	1661.05
Case II	6	12	–0.25	965.43
Case III	6	–12	0.25	914.42
Case IV	6	–12	–0.25	1028.70
Case I	7	12	0.25	1372.30
Case II	7	12	–0.25	1189.24
Case III	7	–12	0.25	761.50
Case IV	7	–12	–0.25	1422.35

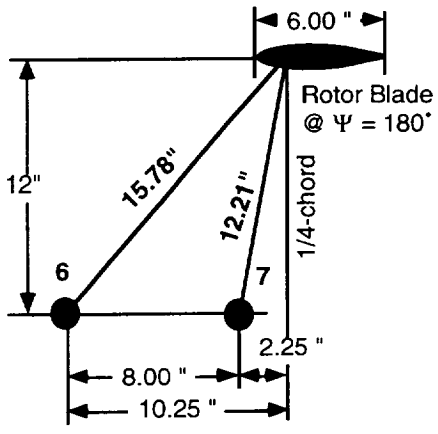

Figure 4.2 Location of microphones 6 and 7 with respect to the rotor quarter-chord at the rotor 88 percent radius.

Table 4.2 Expected arrival time (as computed by linear theory) in blade azimuth angle for peak pressure amplitudes to reach each microphone location

Linear theory peak sound arrival time in rotor blade azimuth angle		
	$M_{tip} = 0.6$	$M_{tip} = 0.7$
Mic 6	193.3°	195.3°
Mic 7	190.3°	191.9°

For Cases I and III (CCW vortex rotation), it was noted that the BVI pulse had a positive peak first, whereas Cases II and IV (CW vortex rotation), had a negative peak first. This is expected due to the vortex induced unsteady effective angle of attack on the blade, as described previously in section 1. The CCW rotation first induces an upwash and then a downwash, whereas the CW rotation induces a downwash first, then an upwash. For Cases I and III (CCW) the first peak is small as compared to the second peak, whereas for Cases II and IV (CW), the positive and negative peaks are similar in magnitude.

The asymmetry is due to the addition of thickness effects, which is primarily a negative pressure. Thickness effects alone were not measured in the experiment, so this effect could not be separated from the BVI experimental data. Also, in addition to waveform symmetry expected within each plot, there is symmetry expected between the test cases. Cases I and IV, and Cases II and III, are expected to be nearly equal and opposite of each other since their test conditions are nearly mirror images (except microphone location). Computationally, thickness effects can be removed, and it is illustrated in section 4.4 that the cases show the more symmetrical pattern, both within each waveform and between the cases, when the effects of thickness are removed.

The sound pressure time histories measured for Case I, microphone 6, at $M_{tip} = 0.7$, and Case III, microphone 7, at $M_{tip} = 0.7$, were slightly different from expected trends. Case I, microphone 6, had an unexpectedly high peak-to-peak amplitude and Case III, microphone 7, was unexpectedly low in amplitude. A slight increase or decrease was anticipated depending on the horizontal induced velocity the vortex created on the blade, due to compressibility effects. If the induced velocity (shown as horizontal arrows in fig. 2.6) opposed the freestream velocity, this decreased the local forces felt by the blade and a reduction in peak-to-peak pressure amplitude was expected. Conversely, an induced velocity in the same direction as the freestream would increase the pressure change. However, the magnitude of change seen in the experimental data for these two cases was slightly greater than expected, and the deviation is unexplained at this time.

4.2 Comparison of CFD and Experiment

In the present study, the TURNS code was used to calculate near-field acoustic pressures at the specific microphone locations and test conditions for the test in the ARC 80- by 120-Foot Subsonic Wind Tunnel experiment, as discussed in section 2. All the experimental and computational results are presented together for each case and microphone in Appendix B. Specific cases that represent the general trends of all of the data are now discussed.

It was observed that in all cases, the computational model produced results that followed the qualitative trends of the experimental data very well. The basic waveshape of the time histories was consistent with each experimental case, and the slopes of the impulsive noise, which is important for acoustics, was matched nearly exactly. However, in the majority of the cases examined, the CFD model significantly overpredicted the peak-to-peak amplitude of the sound pressure. The percent difference between the experiment and CFD (Percent Diff = [(Exp–CFD)/Exp]100) was between –3 and +56 percent (equivalent to 0.3 dB and 3.9 dB, respectively), depending on the case, but was generally about 30 percent (2.3 dB).

Table 4.3 lists the peak-to-peak amplitudes for both the experiment and CFD, and the percentage difference between these results. As mentioned previously, the experimental data for Case I, microphone 6, and Case III, microphone 7, both at $M_{tip} = 0.7$, had an unusually high and low peak-to-peak amplitude, respectively. Therefore, the corresponding CFD calculations underpredicted and overpredicted those cases. The consistent overprediction by the CFD lead to the investigation of vortex strength, and will be discussed in section 4.4.

In all of the computed results, oscillations were noted for the 210 deg to 240 deg azimuthal region. These were not evident in the experimental data. The unaveraged experimental data (fig. 2.7) does show some high frequency "noise" after the BVI event, but to a much smaller degree. Oscillations in the computational data can be seen clearly in the 210 to 240 deg region in figure 4.3. It was suspected that the fluctuations were due to numerical errors in the computational model, and motivated an examination into the effects of increased time accuracy. The results of increased time accuracy are discussed in section 3.5.

In many of the compared cases, it was observed that there was a phase shift between the CFD maximum and minimum peaks and those peaks in the experimental data. This is most likely due to the location of the interaction being somewhere other than the quarter-chord as computations assume. In addition, some degree of deviation with the measured data was expected due to limitations in the data acquisition and experimental set-up. For example, the 1/revolution data acquisition trigger, used to record experimental data, was suspected of being slightly inconsistent (ref. 44). For $M_{tip} = 0.6$, in Cases I and IV, the CFD main BVI event occurred about 5 deg sooner than in the experimental results. For $M_{tip} = 0.7$, the same phase shift existed in Cases I, II, and IV. The amount of shift for microphones 6 and 7 was the same for all cases where a phase shift was present. This lead to the estimation of experimental phase error of ±4 deg. The time at which the BVI event occurs is trivial in comparison to the loudness, measured by amplitude, and impulsiveness, measured by slope. As previously mentioned, the experimental amplitude error was estimated at 5 percent of the peak-to-peak amplitude due to averaging. Figure 4.3 illustrates a typical case where the overprediction and phase shift were seen.

Table 4.3 Peak-to-peak amplitudes for CFD calculations with a nondimensional vortex strength of 0.406 and difference from experimental results

M_{tip} = 0.6	Mic	α_v	Z_v	Experiment	CFD $\hat{\Gamma}$ = 0.406	% Diff. in Pascals	Diff. in dB
Case I	6	12	0.25	786.12	964.08	22.64	1.77
Case II	6	12	–0.25	549.73	851.88	54.96	3.80
Case III	6	–12	0.25	634.35	814.92	28.47	2.18
Case IV	6	–12	–0.25	575.83	861.85	49.67	3.50
Case I	7	12	0.25	708.58	925.48	30.61	2.32
Case II	7	12	–0.25	722.66	962.81	33.23	2.49
Case III	7	–12	0.25	575.51	845.10	46.84	3.34
Case IV	7	–12	–0.25	825.94	1078.72	30.61	2.32
M_{tip} = 0.7	Mic	α_v	Z_v	Experiment	CFD $\hat{\Gamma}$ = 0.406	% Diff. in Pascals	Diff. in dB
Case I	6	12	0.25	1661.05	1606.59	–3.28	–0.29
Case II	6	12	–0.25	965.43	1399.73	44.99	3.23
Case III	6	–12	0.25	914.42	1191.72	30.33	2.30
Case IV	6	–12	–0.25	1028.70	1414.18	37.47	2.76
Case I	7	12	0.25	1372.30	1343.25	–2.12	–0.19
Case II	7	12	–0.25	1189.24	1427.71	20.05	1.59
Case III	7	–12	0.25	761.50	1192.54	56.60	3.90
Case IV	7	–12	–0.25	1422.35	1677.39	17.93	1.43

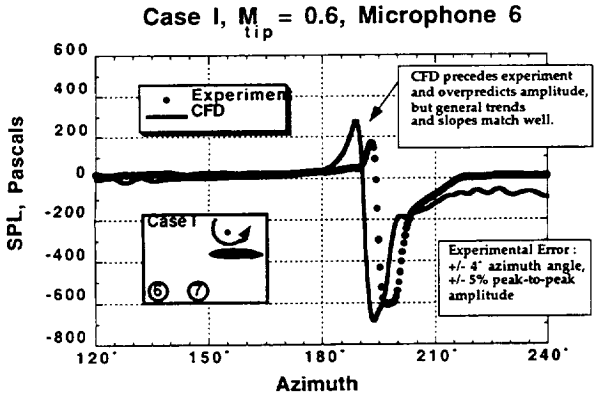

Figure 4.3 Comparison of experimental and computational results for Case I, M_{tip} = 0.6, microphone 6.

The phase shift, however, was not present in all cases. Figure 4.4 illustrates a clockwise vortex rotation (Case II) where the experiment and CFD maximum peak occurs at the same time, near Ψ = 193 deg. For Case IV, also with clockwise rotation and shown in figure 4.5, the CFD maximum peak was again at Ψ = 193 deg, but the experimental results indicate the maximum peak occurring a few degrees later. This implies that the CFD predictions are consistent in time, and it is the experimental data that varies. The linear theory, shown in table 4.2 earlier, predicts that the maximum peak should occur near the 193 deg azimuth angle in both cases. In all cases showing a phase shift, the difference between the two cases is less than the ±4 deg estimated error for the experiment. In addition, the time at which the BVI noise occurs is not particularly relevant to the comparison of the sound characteristics, that is; amplitude and impulsiveness.

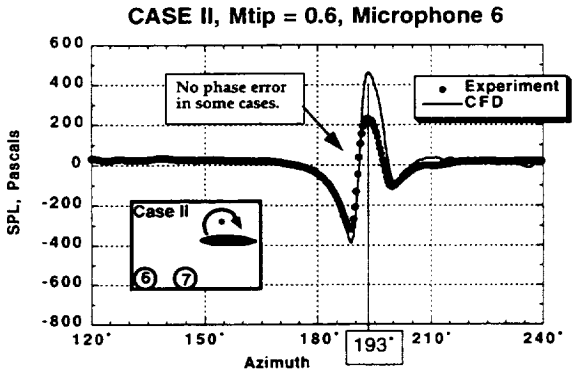

Figure 4.4 Comparison of experimental and computational results for Case II, M_{tip} = 0.6, microphone 6.

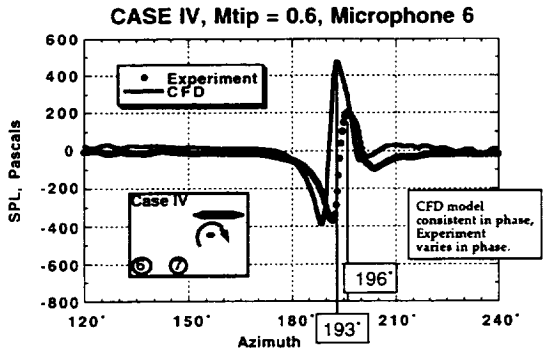

Figure 4.5 Comparison of experimental and computational results for Case IV, M_{tip} = 0.6, microphone 6

4.3 Thickness Effects

The CFD calculations were also run without initializing the vortex into the flow. This enabled the calculation of pressure changes due to aerodynamic disturbances and thickness noise, without any BVI event. (The CFD calculations of thickness effects have been extremely valuable, since data of this nature was not obtained during the experiment.) The results obtained without the vortex are subtracted from the results obtained with the vortex in order to examine the effects caused solely by the changing lift from the BVI.

Figure 4.6(a)(b) show the CFD calculation of thickness effects at the two near-field microphone locations for both tip Mach numbers. Figure 4.6(a) is the time history of the aerodynamic disturbance caused by the passing rotor blade (without the line vortex present) for microphone 6, and figure 4.6(b) is the time history for microphone 7.

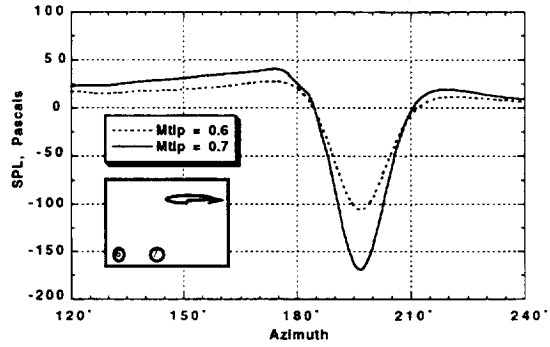

(a) Microphone 6

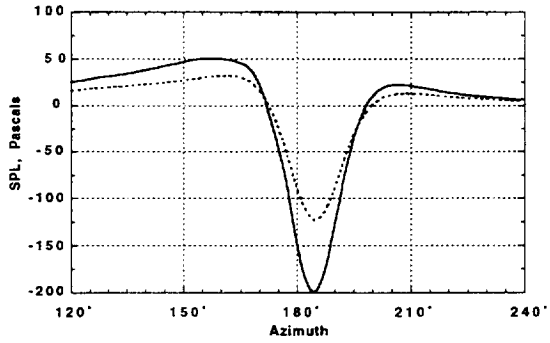

(b) Microphone 7

Figure 4.6 CFD calculations of thickness effects (without vortex) for microphones 6 and 7 at M_{tip} = 0.6 and 0.7.

The solid and dashed lines represent the hover Mach tip numbers of 0.6 and 0.7, respectively.

Thickness effects always have a predominantly wide and negative pressure time history (ref. 2) whereas the BVI event has both positive and negative sharp peaks. Thickness noise distorts the BVI signal by decreasing the positive peaks, increasing the negative peaks, and causing some slopes to decrease (appear more gradual). Also, the pressure disturbance from thickness can arrive at the microphones at a different time than the BVI noise. It was mentioned in section 4.2 that the BVI sound event propagates at the speed of sound, but the aerodynamic disturbance travels mainly with the blade rotation.

Figure 4.7 is shown to help illustrate that the blade first encountered the vortex at the Ψ = 180 deg, then, as it passed over microphone 7 at Ψ = 183 deg, the BVI propagated quickly to both mics, and then the rotor passed over microphone 6, at 195 deg. This is why the pressure disturbance from thickness is seen in the first half of the

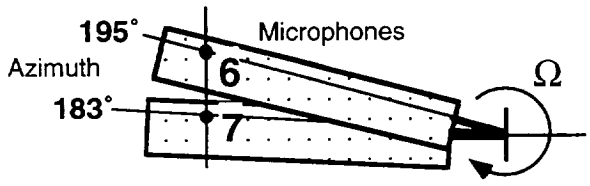

Figure 4.7 Schematic of microphone locations with respect to rotor quarter-chord azimuth angle, and 88 percent rotor radius.

BVI event for microphone 7, and in the second half for microphone 6.

As previously mentioned, thickness effects can be removed from the computed data simply by subtracting the results for no vortex in the flow from the results with the vortex in the flow. Figure 4.8 shows the computed pressure time histories at microphones 6 and 7 for $M_{tip} = 0.7$, with the thickness effects removed. Here, it is clearly visible that Case I has a pressure time history that is nearly equal in magnitude and opposite in sign as Case IV. This is expected because the geometry of the interactions (except the microphones) are mirror images of each other. For Cases II and III the wave shapes are nearly equal and opposite for the microphone 7 location, but a weaker BVI pulse is observed at microphone 6 for Case III.

It was mentioned in section 4.1 that the experimental data did not show a symmetric BVI signature due to thickness effects. Symmetry is expected within each plot, with the positive pulse nearly equal and opposite to the negative pulse, and an entire time history waveform, in certain cases, being a mirror images of another (Cases I and IV, and II and III). It is seen here, that after thickness effects are removed, the time histories indicate more closely the expected symmetry.

4.4 Effect of Vortex Parameters on CFD Results

The results showed that the CFD consistently over-predicted the experimental data by approximately 30 percent and the vortex modeling is considered to be a possible source of error. The computations assume the line vortex in the experiment is stationary, and has the exact strength, size, and location as specified by the input values.

The Euler solver assumes that the line vortex remains undisturbed from its streamwise path, and it is questionable whether this accurately models the vortex structure and location. This assumption implies that the vortex remains undistorted in velocity profile and unwavering in location, which was not the case in the experiment as observed by smoke flow visualization. The vortex tended to follow streamlines of the flow environment, and was slightly distorted by the interaction with the rotor. In addition, the rotor itself is affected by the sheet wake of the vortex generator when the wing was positioned to generate a vortex above the rotor.

Kitaplioglu et al. (ref. 17) found that an increase in vortex distance (farther from the blade) of a quarter-chord, produces a 35 percent reduction in peak acoustic pressure (ref. 18). Therefore, it is possible that the vortex was not in the exact position specified, which would affect the BVI amplitude and phasing.

It is also unclear at this time as to what effect different vortex velocity models would have on the near-field pressure time histories. Most investigators have determined the vortex strength and core radius to implement in CFD codes by matching the location and magnitude of the maximum tangential velocity of the experiment with those corresponding to the vortex core model. Such a choice guarantees good agreement near the core radius for any chosen model, but different models can produce dramatically different results as one moves away from the core (due to different predicted strengths). For example, the Scully vortex model (ref. 47) results in tangential velocities far away from the vortex core that are only half those due to the more common Rankine vortex if the maximum tangential velocities are identical. In addition, the models produce dramatically different rates of drop-off in the tangential velocity as one moves radically outward (possibly more important for acoustic noise generation). Is it better to match the inner peak velocity or the outer vorticity? The determination of a suitable vortex model is still the subject of research.

McAlister and Takahashi (ref. 41) made extensive flow measurements of the vortex strength for the NACA 0015 wing. There is some question regarding an appropriate value of the nondimensional vortex strength, since it was not measured directly in the ARC 80- by 120-Foot Subsonic Wind Tunnel experiment. It was mentioned in section 3.4 that Caradonna et al. (ref. 15) working with similar data, used a $\hat{\Gamma} = 0.406$, as was used here. However, McAlister and Takahashi specify a nondimensional vortex strength of 0.35 for the $\alpha_v = \pm 12$ deg cases. All of the computational data in Appendix B is calculated with $\hat{\Gamma} = 0.406$, but two cases, presented in this section, were calculated with the $\hat{\Gamma} = 0.35$.

In order to determine the effect of modifying vortex strength, the CFD code was rerun for Cases I and IV, with $\hat{\Gamma} = 0.35$ and $M_{tip} = 0.7$. The resulting time histories at microphones 6 and 7 are shown in figure 4.9. Peak-to-peak values were reduced by approximately 15 percent, as listed in table 4.4. This greatly improves the quantitative

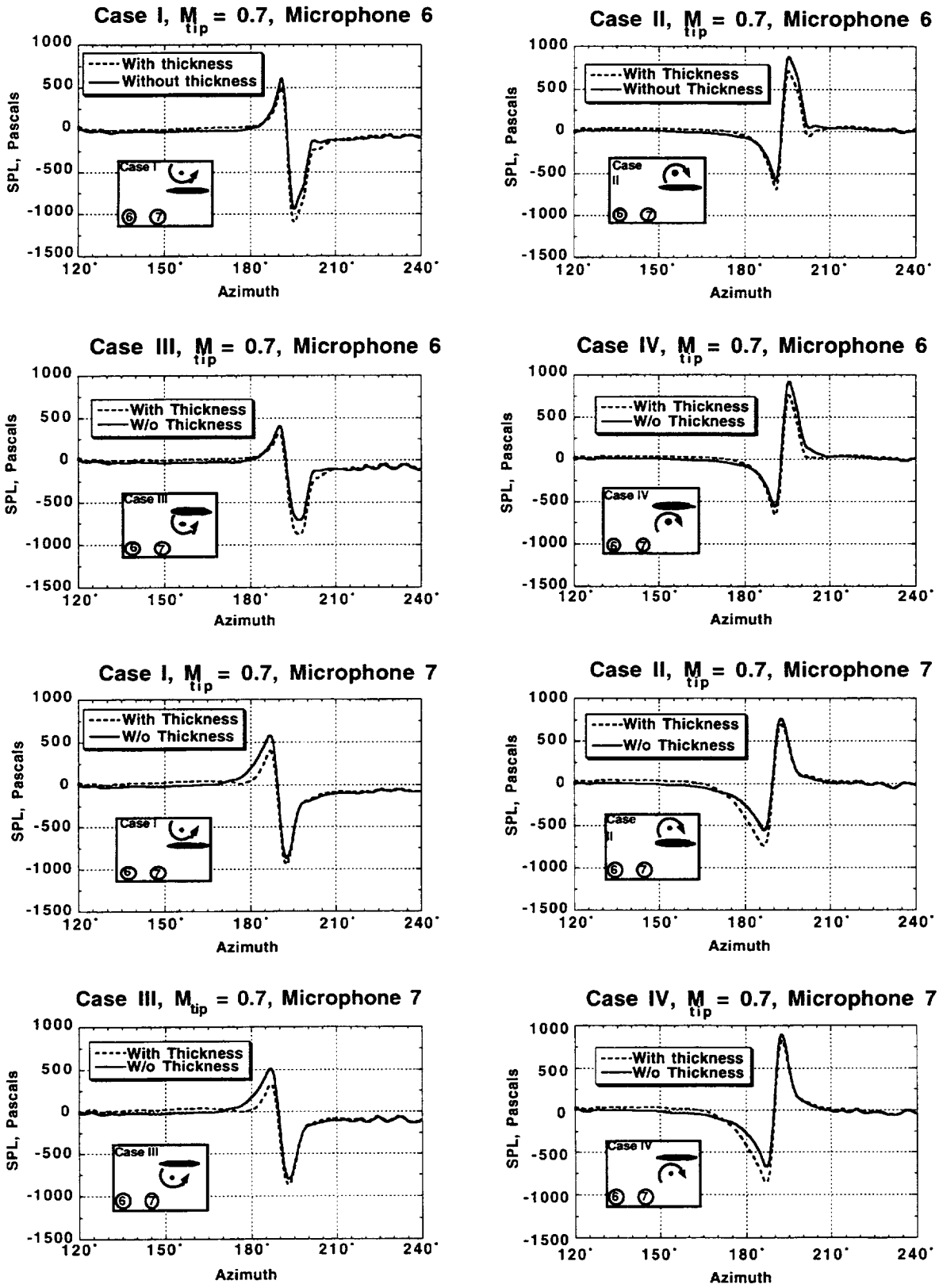

Figure 4.8 CFD calculations with and without thickness effects for M_{tip} = 0.7.

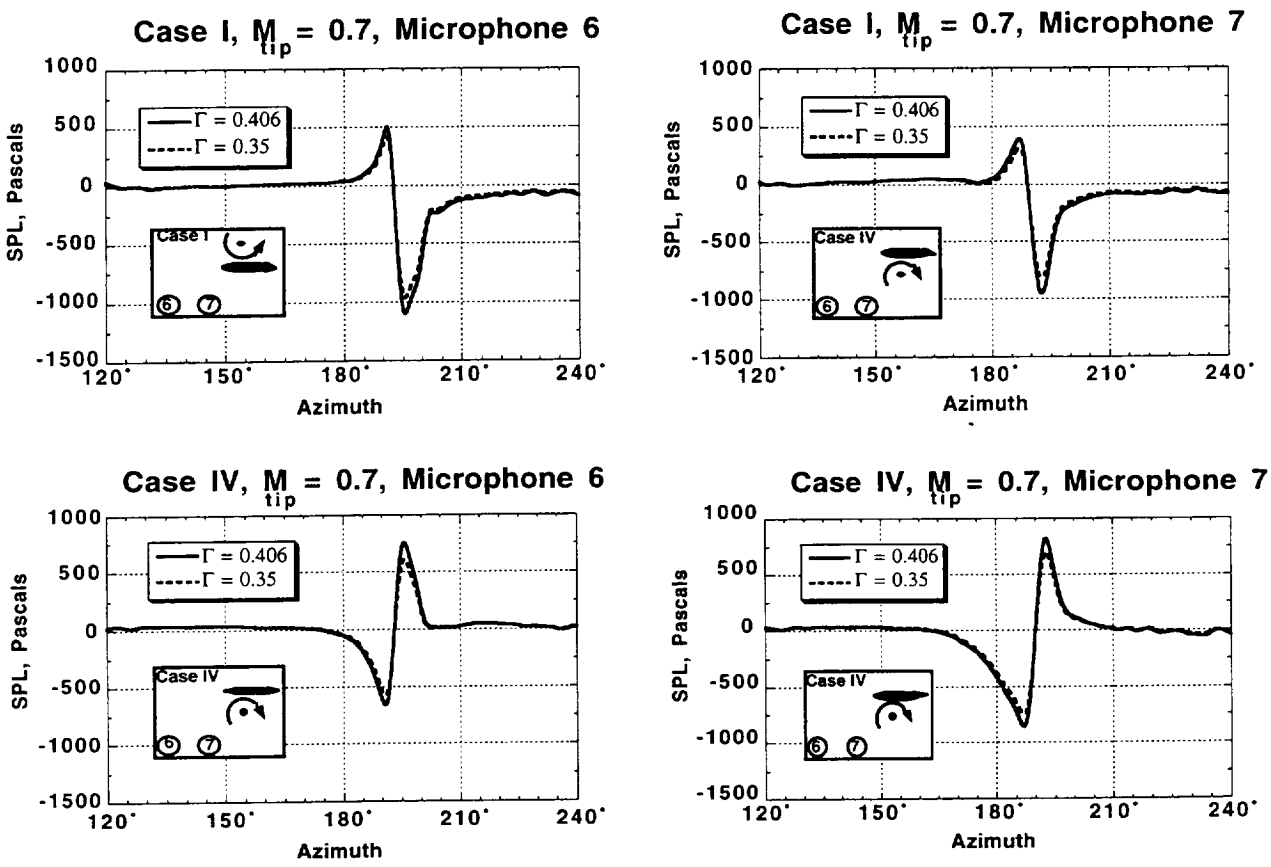

Figure 4.9 Effect of vortex strength on CFD calculations with $\hat{\Gamma}$ = 0.406 and 0.35, for Cases I and IV at M_{tip} = 0.7 and with thickness effects removed.

agreement with experiment for Case IV. However, Case I was then underpredicted by approximately 17 percent.

The 15 percent reduction in peak-to-peak values is very close to the percent reduction in vortex strength, therefore, it appears that the reduction in peak-to-peak amplitude is proportional to vortex strength, and nonlinear effects are insignificant. The smaller vortex strength of $\hat{\Gamma}$ = 0.35 is 86.21 percent of the $\hat{\Gamma}$ = 0.406 used earlier, and resulted in an average change in peak-to-peak amplitude (without thickness effects) of 85.21 percent. The data noted with an asterisk (*) in table 4.4 indicates the peak-to-peak value was obtained by multiplying the previously calculated amplitude ($\hat{\Gamma}$ = 0.406) by a factor of 0.8521 to determine the amplitude expected for a vortex strength of 0.35. The nearly linear relation implies that the nonlinear effects in this region are small and that a linear model may be sufficient for determining the peak-to-peak pressure amplitudes.

The smaller vortex strength improved the correlation of peak-to-peak amplitude with experiment for most cases. However, the true value of the vortex strength in the experiment is uncertain and so the corresponding strength for the computational model is uncertain as well.

4.5 Effect of Newton Sub-Iterations

A review of the preliminary results indicated an over-prediction of the experimental data, and showed some oscillations in the time history occurring between 210 and 250 deg azimuth angle. A study was done to investigate the effects of increased time accuracy in the CFD calculations in order to reduce numerical oscillations seen in the computed time histories. These oscillations, which occurred well after the BVI event, could be caused by numerical approximations, and may be reduced by increased time accuracy.

Table 4.4 Peak-to-peak pressure amplitude comparisons

Test conditions				Peak-to-peak pressure amplitude in Pascals				
$M_{tip} = 0.6$	Mic	α_v	Z_v	Experiment	CFD $\hat{\Gamma} = 0.406$ 5 s.i.†	$\hat{\Gamma} = 0.406$ 5 s.i. w/o thickness	$\hat{\Gamma} = 0.35$ 5 s.i. w/o thickness	$\hat{\Gamma} = 0.406$ 3 s.i.
Case I	6	12	0.25	786.12	964.08	916.60	781.03*	1053.30
Case II	6	12	–0.25	549.73	851.88	899.34	766.32*	940.80
Case III	6	–12	0.25	634.35	814.92	749.20	638.39*	864.15
Case IV	6	–12	–0.25	575.83	861.85	910.59	775.91*	936.85
Case I	7	12	0.25	708.58	925.48	971.51	827.82*	1026.07
Case II	7	12	–0.25	722.66	962.81	921.13	784.89*	1073.32
Case III	7	–12	0.25	575.51	845.10	897.74	764.96*	912.56
Case IV	7	–12	–0.25	825.94	1078.72	1035.64	882.47*	1206.99
$M_{tip} = 0.7$	Mic	α_v	Z_v	Experiment	CFD $\hat{\Gamma} = 0.406$ 5 s.i.	$\hat{\Gamma} = 0.406$ 5 s.i. w/o thickness	$\hat{\Gamma} = 0.35$ 5 s.i. w/o thickness	$\hat{\Gamma} = 0.406$ 3 s.i.
Case I	6	12	0.25	1661.05	1606.59	1544.06	1326.61	1717.33
Case II	6	12	–0.25	965.43	1399.73	1462.25	1245.98*	1537.59
Case III	6	–12	0.25	914.42	1191.72	1114.92	950.02*	1220.35
Case IV	6	–12	–0.25	1028.70	1414.18	1486.71	1252.30	1500.05
Case I	7	12	0.25	1372.30	1343.25	1450.07	1242.16	1457.26
Case II	7	12	–0.25	1189.24	1427.71	1309.47	1115.80*	1565.80
Case III	7	–12	0.25	761.50	1192.54	1305.80	1112.67*	1268.22
Case IV	7	–12	–0.25	1422.35	1677.39	1571.31	1335.96	1809.56

*Value obtained by linear relation. See section 4.4.

†s.i. = Newton sub-iterations.

Initial calculations were made using three Newton sub-iterations (see Appendix A for a description of the scheme). It was found that increasing the maximum number of sub-iterations to five reduced the peak-to-peak amplitudes slightly, and the oscillations after the BVI event were reduced slightly. Since a constant time step was used it was expected that the largest errors due to linearization and factorization may occur when the vortex was in the vicinity of the rotor blade. There was a need for more sub-iterations during this interval to guarantee that the time accuracy was truly second order. Figure 4.10 shows the effect of the Newton sub-iterations on the computations for Cases I and IV at $M_{tip} = 0.7$. Increasing the number of maximum Newton sub-iterations above five had little additional effect. It was concluded that the increased time accuracy was necessary in the area of the BVI event, but that the oscillations in the pressure time history were not numerical errors.

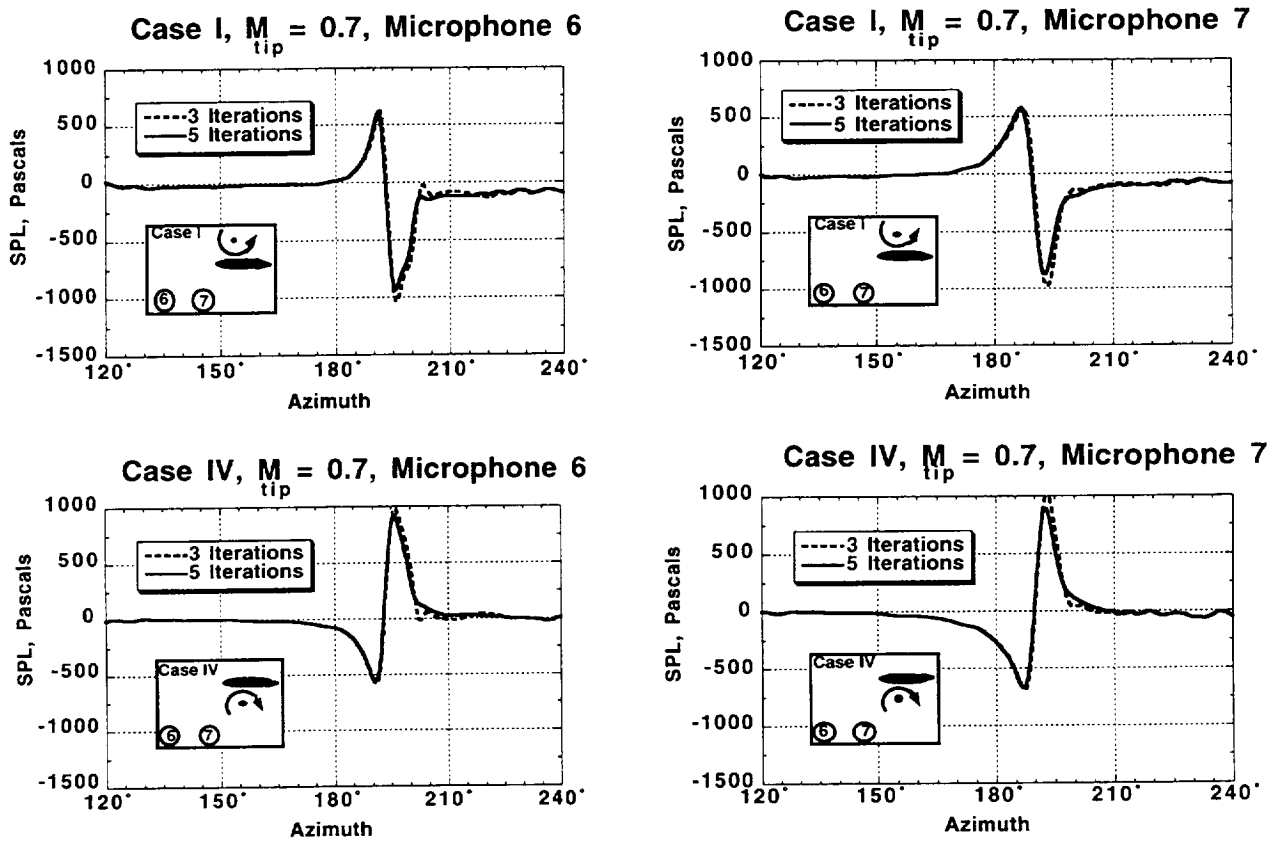

Figure 4.10 Effect of Newton sub-iterations on CFD calculations using 3 and 5 sub-iterations for Cases I and IV at M_{tip} = 0.7 and with thickness effects removed.

4.6 Study of Directionality

The advantage of computational acoustic studies is that an unlimited number of "microphone" locations are available for investigation. To take advantage of this feature, additional locations were examined for one case, in addition to those of microphones 6 and 7 in the wind tunnel experiment. This was done to study the calculated directionality of the BVI acoustics. That is, in which direction does the BVI noise propagate most strongly?

First, microphones 6 and 7 were examined for M_{tip} = 0.6, Case III, shown in figure 4.11. Thickness effects were removed from the data, so the differences are only due to microphone location. Microphone 7 is clearly seen to receive a stronger BVI signature. However, microphone 7 is physically closer to the event than microphone 6, so it is unclear whether the stronger signal is due to that decreased distance or because of the nature of the wave propagation, as mentioned in sections 3.4 and 4.3.

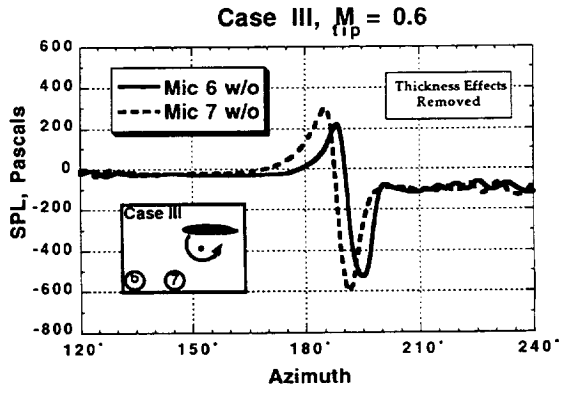

Figure 4.11 Computational results of microphones 6 and 7 with thickness effects removed for Case III, M_{tip} = 0.6.

Twelve additional microphone locations were chosen at 15 deg increments down from the rotor plane (as defined from the rotor quarter-chord and 88 percent radius when the rotor is at Ψ = 180 deg) at two different distances from the rotor quarter-chord, as illustrated in figure 4.12. The first array ("a") was 15.78 in. away from the rotor quarter-chord, as was microphone 6.

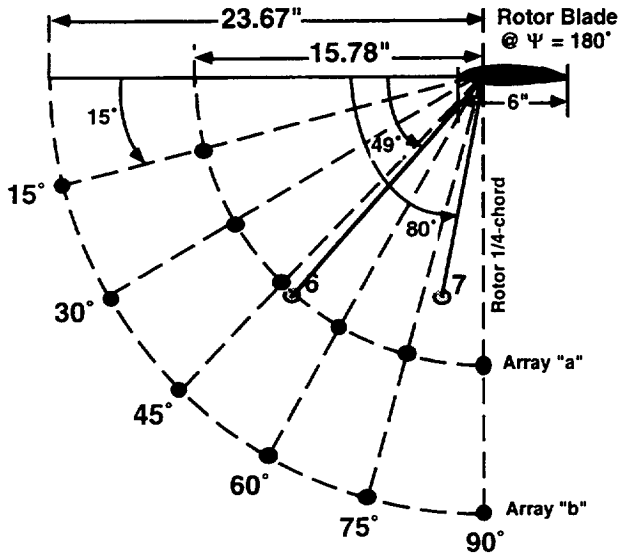

Figure 4.12 Schematic of location of microphones with respect to the rotor quarter-chord, at 0.88R, when the rotor is at Ψ = 180 deg.

The second array ("b") was 50 percent farther, at 23.67 in. away from the rotor quarter-chord. (Additional arrays at further distances were not examined since the grid becomes coarse and the results become questionable beyond four chord lengths from the rotor surface.)

The microphones in each array are equidistant from the rotor quarter-chord at .88R, when the rotor is at Ψ = 180 deg, and with thickness effects removed, the only differences between these microphones is the angle below the rotor plane. Peak-to-peak pressure amplitudes in Decibels were calculated, with thickness effects removed, for the microphones shown in figure 4.12, for Case III at M_{tip} = 0.6 (the same case as shown in fig. 4.11).

The results showed that the maximum pressure was near the 60 deg angle at both distances. However, if the microphones are examined from a side view, as shown in figure 4.13, and the radiation is measured from the rotor hub, the maximum amplitudes are at angles of 23 and 33 deg.

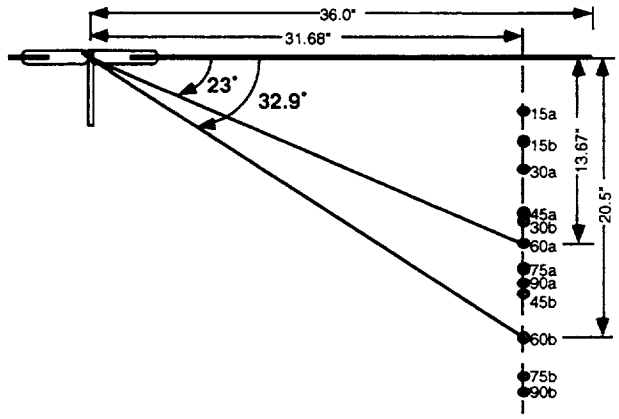

Figure 4.13 Microphone locations with respect to rotor hub. (Microphone numbers refer back to locations shown in fig. 4.12.)

The peak-to-peak pressure amplitudes (in Decibels) for all the microphones measured from the two different reference points are shown in figure 4.14. The squares and circles indicate the microphones in the "a" and "b" arrays, respectively. The solid lines indicates angles were measured from the rotor quarter-chord at .88R when the rotor is at Ψ = 180 deg, and the dashed lines indicate the angle is measured from the rotor hub. As previously mentioned, it can be seen in the data measured from the rotor quarter-chord that the maximum amplitude occurs at 60 deg at both distances, and for the data measured from the rotor hub, the maximum values occur at 23 and 33 deg. Theory suggests that the far-field radiation of BVI noise is most dominant in the 30 deg to 45 deg range, as

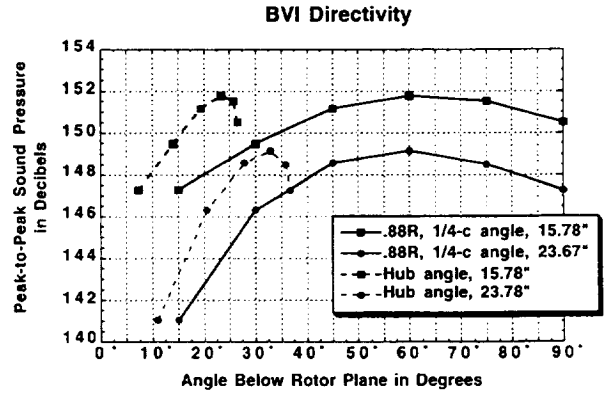

Figure 4.14 Computational BVI directivity (peak-to-peak amplitudes) as measured from two separate reference points.

measured down from the rotor hub (ref. 2). The BVI noise does, in fact, radiate from near the rotor tip, but the far-field propagation (several rotor diameters) is most easily measured from the rotor hub. Since these microphones are in the near-field, the angles measured from both reference points are deceiving, and an angle somewhere between the two would most likely represent what would be most dominant in the far-field. If this is the case, the angles measured here, between 23 and 60 deg, would converge to angles within the expected 30 to 45 deg in the far-field.

4.7 Summary of Results

Experimental BVI data has been presented for eight test cases. The acquisition and analysis process has lead to the determination of an experimental error of ±4 deg azimuth angle, and 5 percent peak-to-peak amplitude error. In all cases, the BVI event was recorded earlier by microphone 7 due to its closer proximity to the blade, when the blade was at 180 deg. Two basic trends were observed in the experimental data. In the CCW vortex rotation, Cases I and III, the BVI pulse had a positive peak first (due to the up or downwash induced by the vortex) and a gradual slope (due to the non-propagating thickness noise) which was seen after the BVI event. In the CW cases, there was a negative peak first and a gradual slope before the BVI event. Also, in the CCW rotation, microphone 6 recorded a higher peak-to-peak pressure amplitude, despite its more distant location, due to the directionality of the BVI signal in those cases.

Calculated CFD pressure time histories at simulated microphone positions for a rotor undergoing BVI were compared to the experimentally measured acoustics data for eight test cases. The computational results were found to match the general trends very well, capturing waveshapes and slopes accurately. However, the CFD model consistently overpredicted the peak-to-peak amplitudes in the experiment. The input of a reduced vortex strength from more recent references reduced the amount of overprediction, but a significant error still existed. There was also an occasional small phase shift observed between the computational and experimental data, but this difference was determined to be within the bounds of experimental uncertainty and unimportant to the acoustics of the BVI.

Additional CFD calculations were made to study thickness effects, the effect of vortex strength and Newton sub-iterations on the CFD results and the effect of directionality. Thickness effects were found to obscure BVI characteristics and were therefore subtracted the CFD data. Unfortunately, experimental thickness noise data were not available, and it was not possible to study the recorded BVI noise without the effect of thickness. The computational vortex strength related almost linearly to the calculated BVI peak-to-peak amplitude. In addition, increased time accuracy was found to be necessary only in the region of BVI. Also, the effects of directionality were isolated by using CFD to investigate microphone locations that were equidistant from the rotor. In Case III, for $M_{tip} = 0.6$, microphones calculated to have the highest peak-to-peak pressure amplitude were at 60 deg below the rotor plane, as measured from the rotor quarter-chord, and 23 and 33 deg below the rotor plane, as measured from the hub.

5 Summary and Conclusions

5.1 Summary

This report has provided a detailed comparison of the ARC 80- by 120-Foot Subsonic Wind Tunnel near-field microphone data with CFD calculations for a quantitative evaluation of predicted BVI acoustics. The experiment was tailored to control the parameters affecting BVI noise and offered a simplified flow environment that CFD could simulate. The purely CFD method offered one of the first off-surface predictions for comparison. The results show excellent qualitative comparison, but quantitatively, there is an overprediction in amplitude and a phase shift in some cases.

There are several sources of uncertainty that could have contributed to this disagreement. The "free" vortex strength and structure, although measured on the same wing previously, was not directly measured in this experiment. Therefore, it is possible that the strength and structure could have been slightly different than previously measured, and this could affect the results. It was also noted that the CFD assumes the vortex location is constant, whereas in the experiment, the vortex would most likely follow a streamline, slightly changing its miss distance relative to the blade. Therefore, a likely cause for discrepancies between the experiment and CFD could be deficiencies in the vortex modeling and trajectory used in the CFD computations.

5.2 Conclusions

The following conclusions have been made:

1. Near-field thickness effects can obscure the true BVI noise signature and should be removed from both experimental and computational data in order to more completely isolate the BVI noise.

2. A reduction in the nondimensional vortex strength from 0.406 to McAlister and Takahashi's recommended value of 0.35 in the computational model reduced the peak-to-peak amplitudes by 15 percent. This reduced the original 30 percent (2.4 dB) overprediction to a 15 percent (1.2 dB) overprediction. The algebraic vortex model used in the code could also be a source of the amplitude error.

3. The occasional phase difference between the CFD predictions and experiment is believed to be a result of the parallel interaction occurring at the leading edge of the blade as opposed to the 1/4-chord as assumed in the CFD calculations.

4. This work has demonstrated that a purely CFD method could be used to investigate the initial propagation and noise from an interaction of an isolated vortex with a rotor blade. The computed CFD solution provides a rich numerical database for examining the initial development and propagation of BVI noise.

Appendix A

Computational Fluid Dynamics Model

Governing Equation

The Cartesian coordinate system (x, y, z, and t) is attached to the inertial frame, and the corresponding velocity components are u, v, w, and t is time. Pressure, density, and total energy per unit volume are represented as p, ρ, and e, respectively. The three-dimensional (3-D), unsteady Euler equations and the energy equation are in the time-dependent curvilinear coordinate system:

$$\begin{aligned} \xi &= \xi(x,y,z,t) \\ \eta &= \eta(x,y,z,t) \\ \zeta &= \zeta(x,y,z,t) \\ \tau &= t \end{aligned} \tag{A.1}$$

The conservation law form of the Euler equations in the curvilinear coordinate system is:

$$\frac{\partial Q}{\partial \tau} + \frac{\partial E}{\partial \xi} + \frac{\partial F}{\partial \eta} + \frac{\partial G}{\partial \zeta} = 0 \tag{A.2}$$

where Q is the conserved quantities:

$$Q = \frac{1}{J}\begin{bmatrix} \rho \\ \rho u \\ \rho v \\ \rho w \\ e \end{bmatrix} \tag{A.3}$$

and E, F, and G are the inviscid fluxes:

$$E = \frac{1}{J}\begin{bmatrix} \rho U \\ \rho u U + \xi_x p \\ \rho v U + \xi_y p \\ \rho w U + \xi_z p \\ U(e+p) - \xi_t p \end{bmatrix}, \quad F = \frac{1}{J}\begin{bmatrix} \rho V \\ \rho u V + \eta_x p \\ \rho v V + \eta_y p \\ \rho w V + \eta_z p \\ V(e+p) - \eta_t p \end{bmatrix},$$

$$G = \frac{1}{J}\begin{bmatrix} \rho W \\ \rho u W + \zeta_x p \\ \rho v W + \zeta_y p \\ \rho w W + \zeta_z p \\ W(e+p) - \zeta_t p \end{bmatrix} \tag{A.4}$$

The Jacobian of the transformation, J, is defined as:

$$J = \frac{\partial(\xi,\eta,\zeta)}{\partial(x,y,z)}$$

$$J = \begin{bmatrix} x_\xi\left(y_\eta z_\zeta - z_\eta y_\zeta\right) - y_\xi\left(x_\eta z_\zeta - z_\eta x_\zeta\right) \\ + z_\xi\left(x_\eta y_\zeta - y_\eta x_\zeta\right) \end{bmatrix}^{-1} \tag{A.5}$$

and U, V, and W are the contravariant velocities:

$$\begin{aligned} U &= \xi_x u + \xi_y v + \xi_z w + \xi_t \\ V &= \eta_x u + \eta_y v + \eta_z w + \eta_t \\ W &= \zeta_x u + \zeta_y v + \zeta_z w + \zeta_t \end{aligned} \tag{A.6}$$

The equation of state is:

$$p = (\gamma - 1)\left\{e - \frac{\rho}{2}\left(u^2 + v^2 + w^2\right)\right\} \tag{A.7}$$

Numerical Algorithm

The Transonic Unsteady Rotor Navier–Stokes (TURNS) algorithm is based on an upwind-biased, flux-difference scheme for evaluation of the inviscid fluxes. The upwinding, originally developed by Roe (ref. 48), eliminates the addition of explicit numerical dissipation. The van Leer Monotone Upstream-centered Scheme for the Conservation Laws (MUSCL) (ref. 49) approach is used to obtain higher order accuracy with flux limiters on the right hand side of the equation. The Lower-Upper-Symmetric Gauss-Seidel (LU-SGS) scheme (ref. 50) is used for the implicit operator on the left hand side. These features provide high order accuracy and make the code computationally efficient and robust.

Space Differencing

The space-discretized form of the differential Euler equations [eq. (A.2)] is:

$$\frac{\partial Q}{\partial \tau} = -\frac{E_{j+1/2} - E_{j-1/2}}{\Delta\xi} - \frac{F_{k+1/2} - F_{k-1/2}}{\Delta\eta} - \frac{G_{l+1/2} - G_{l-1/2}}{\Delta\zeta} \tag{A.8}$$

where i, j, and k correspond to the ξ, η, and ζ coordinate directions, respectively. Roe-upwinding is applied to the numerical flux terms to create a locally one-dimensional (1-D) form. For example, in the ξ direction, the flux at an interface is found to be:

$$E\left[Q_L, Q_R, \left(\nabla\xi/J\right)_{j+1/2}\right]$$

$$= 1/2\left\{E\left[Q_R, \left(\nabla\xi/J\right)_{j+1/2}\right]\right\} + E\left[Q_L, \left(\nabla\xi/J\right)_{j+1/2}\right]$$

$$-\left|A\left[Q_L, Q_R, \left(\nabla\xi/J\right)_{j+1/2}\right]\right|\{Q_R - Q_L\} \tag{A.9}$$

where A is the Roe-averaged flux Jacobian matrix and Q_L and Q_R are the left- and right-hand variables. Equation (A.10) describes the Roe-averaged variables and figure A.1 is an illustration of the E flux space differencing:

$$\rho = \sqrt{\rho_L \rho_R}$$

$$u = \frac{\sqrt{\rho_L}u_L + \sqrt{\rho_R}u_R}{\sqrt{\rho_L} + \sqrt{\rho_R}}$$

$$v = \frac{\sqrt{\rho_L}v_L + \sqrt{\rho_R}v_R}{\sqrt{\rho_L} + \sqrt{\rho_R}} \tag{A.10}$$

$$w = \frac{\sqrt{\rho_L}w_L + \sqrt{\rho_R}w_R}{\sqrt{\rho_L} + \sqrt{\rho_R}}$$

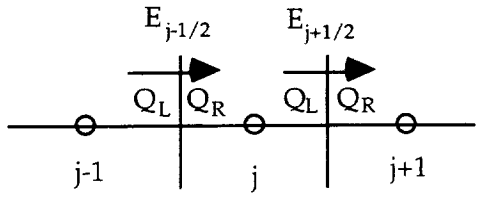

Figure A.1 Schematic of left- and right-flow variables.

A, B, and C are defined similarly by:

$$A \equiv \frac{\partial E}{\partial Q}, \quad B \equiv \frac{\partial F}{\partial Q}, \quad C \equiv \frac{\partial G}{\partial Q} \tag{A.11}$$

A construction of higher order schemes, known as the Monotone Upper Symmetric Conservation Law (MUSCL) scheme (ref. 49), is used for increased accuracy. The higher-order schemes are constructed from a one-parameter family of interpolations for the primitive variables p, ρ, u, v, and w. For example, the left- and right-state variables for p are:

$$P_L = \left\{1 + \frac{\psi_j}{4}[(1-\kappa)\nabla + (1+\kappa)\Delta]\right\}p_j$$

$$P_R = \left\{1 - \frac{\psi_{j-1}}{4}[(1+\kappa)\nabla + (1-\kappa)\Delta]\right\}p_{j+1} \tag{A.12}$$

where Δ and ∇ are backward and forward difference operators, κ is a parameter that controls the construction of higher-order differencing schemes (i.e., κ = 1/3 constructs a third-order scheme) and ψ is a limiter. The limiter is calculated by using Koren's differentiable limiter (ref. 51). For p, this is given by:

$$\psi_j = \frac{3\nabla p_j \Delta p_j + \varepsilon}{2\left(\Delta p_j - \nabla p_j\right)^2 + 3\nabla p_j \Delta p_j + \varepsilon} \tag{A.13}$$

where ε is a small constant (10^{-6}) to prevent division by zero.

Time Discretization and Implicit Formulation

Now that the flux and space differencing are defined, the time is discretized. An implicit formulation is used in order to allow for time steps based on accuracy, not stability. The fluxes, therefore, are evaluated at n + 1 and a backwards difference is used for the time discretization. Q is defined with the flux factors being evaluated in time at n + 1:

$$\frac{Q^{n+1} - Q^n}{\Delta\tau} = -E_\xi^{n+1} - F_\eta^{n+1} - G_\zeta^{n+1} \tag{A.14}$$

The fluxes at time n + 1 are not known and so are linearized about time n:

$$E^{n+1} = E\left(Q^{n+1}\right) = E^n + \left(Q^{n+1} - Q^n\right)\left(\frac{\partial E}{\partial Q}\right)^n + O\left(\Delta\tau^2\right) \tag{A.15}$$

therefore, the derivative of the fluxes can be written as:

$$E_\xi^{n+1} = E_\xi^n + \left(\frac{\partial E}{\partial Q}\Delta Q\right)_\xi + O\left(\Delta\tau^2\right)$$

$$E_\xi^{n+1} = E_\xi^n + (A\Delta Q)_\xi + O\left(\Delta\tau^2\right) \tag{A.16}$$

which leads to:

$$\left[I+\Delta\tau\left(A_\xi^n+B_\eta^n+C_\zeta^n\right)\right]\left(Q^{n+1}-Q^n\right) = -\Delta\tau\left(E_\xi^n-F_\eta^n-G_\zeta^n\right) \quad (A.17)$$

where the term in brackets, [ ], can be expanded by applying flux-splitting that is first order in space:

$$I+\Delta\tau\left(\begin{array}{l}\dfrac{A^+_{j,k,l}-A^+_{j-1,k,l}}{\Delta\xi}+\dfrac{B^+_{j,k,l}-B^+_{j,k-1,l}}{\Delta\eta}\\ +\dfrac{C^+_{j,k,l}-C^+_{j,k,l-1}}{\Delta\zeta}+\dfrac{A^-_{j+1,k,l}-A^-_{j,k,l}}{\Delta\xi}\\ +\dfrac{B^-_{j,k+1,l}-B^-_{j,k,l}}{\Delta\eta}+\dfrac{C^-_{j,k,l+1}-C^-_{j,k,l}}{\Delta\zeta}\end{array}\right) \quad (A.18)$$

Since this matrix is too difficult (or expensive) to invert directly, approximate factorization is used. The matrix can be written as:

$$(D+L+U)\Delta Q^n = \Delta\tau RHS \quad (A.19)$$

where Q are the conserved quantities, the right-hand side (RHS) represents the discretized steady-state terms described in equation (A.9), $\Delta\tau$ is the time step, and n refers to the current time. D implies a matrix with values only on the diagonal, L implies values only in the lower corner, and U corresponds to values only in the upper corner. The addition of matrices D, L, and U, that is D + L + U, is illustrated in figure A.2

$$\begin{bmatrix} D & U & U & U \\ L & D & U & U \\ L & L & D & U \\ L & L & L & D \end{bmatrix}$$

Figure A.2 Illustration of pattern of matrices.

We can rearrange the matrices and apply factorization as follows:

$$\begin{aligned}(D+L+U) &= D\left(I+D^{-1}L+D^{-1}U\right)\\ &\cong D\left(I+D^{-1}L\right)\left(I+D^{+1}U\right)\\ &\cong (D+L)D^{-1}(D+U)\end{aligned} \quad (A.20)$$

to obtain the first order time accurate scheme described as:

$$(D+L)D^{-1}(D+U)\Delta Q^n = -\Delta\tau RHS^n \quad (A.21)$$

Thus, the Lower-Diagonal-Upper factorization used can be regarded as a symmetric Gauss-Seidel relaxation method (ref. 50) and is defined as:

$$\begin{aligned}D+L &= I-\Delta\tau A^-\Big|_{j,k,l}+\Delta\tau\nabla_\xi A^+-\Delta\tau B^-\Big|_{j,k,l}\\ &\quad+\Delta\tau\nabla_\eta B^+-\Delta\tau C^-\Big|_{j,k,l}+\Delta\tau\nabla_\zeta C^+\\ D^{-1} &= \left[I+\Delta\tau\left(A^+-A^-+B^+-B^-+C^+-C^-\right)\Big|_{j,k,l}\right]^{-1}\\ D+U &= I+\Delta\tau A^+\Big|_{j,k,l}+\Delta\tau\Delta_\xi A^-+\Delta\tau B^+\Big|_{j,k,l}\\ &\quad+\Delta\tau\Delta_\eta B^--\Delta\tau C^+\Big|_{j,k,l}+\Delta\tau\Delta_\zeta C^-\end{aligned} \quad (A.22)$$

where $\Delta\tau$ is the time step, and Δ and ∇ represent forward and backward difference operators $(\Delta\xi=\Delta\eta=\Delta\zeta=1)$. To make the scheme computationally more efficient, spectral radius is used to approximate the matrices. For example, the split A matrix, on the LHS, is:

$$A^+ = \tfrac{1}{2}\left(A+I\sigma_\xi\right),\quad A^- = \tfrac{1}{2}\left(A-I\sigma_\xi\right) \quad (A.23)$$

where

$$\sigma_\xi = \left(|U|+ar_\xi\right)(1+\varepsilon),\ \varepsilon=0.01,\ \text{and}\ r_\xi = \sqrt{\xi_x^2+\xi_y^2+\xi_z^2}$$

This simplification makes the D matrix have values only on its diagonal and simplifies its inverse, D^{-1}, to that of inverting only a scalar:

$$D^{-1} = I\left[1+\Delta\tau\left(\sigma_\xi+\sigma_\eta+\sigma_\zeta\right)\right]^{-1} \quad (A.24)$$

Newton Sub-iterations

For unsteady computations, the first order backwards difference in time is combined with Newton type sub-iterations. This reduces the factorization and linearization errors associated with the implicit scheme, the effects of explicit boundary conditions, and restores the full spatial accuracy of the right hand side. P denotes the Newton sub-iteration number in the equation:

$$\left(D^P + L^P\right)\left(D^P\right)^{-1}\left(D^P + U^P\right)\left(Q^{P+1} - Q^P\right)$$

$$= -\Delta\tau\left[\begin{array}{l}\dfrac{Q^P - Q^n}{\Delta\tau} + \dfrac{E^P_{j+1/2} - E^P_{j-1/2}}{\Delta\xi} \\ + \dfrac{F^P_{k+1/2} - F^P_{k-1/2}}{\Delta\eta} + \dfrac{G^P_{l+1/2} - G^P_{l-1/2}}{\Delta\zeta}\end{array}\right] \quad (A.25)$$

where Q^P is an iterative approximation to Q^{n+1}. For the first iteration, P = 0, so $Q^P = Q^n$ and reverts to the conventional non-iterative scheme. When enough iterations of P are used, $Q^{P+1} \approx Q^P \approx Q^{n+1}$ and so the solution approaches solving the equation:

$$\frac{Q^{n+1} - Q^n}{\Delta\tau} + E^{n+1}_\xi + F^{n+1}_\eta + G^{n+1}_\zeta = 0 \quad (A.26)$$

which is first order accurate in time with no factorization or linearization errors.

Newton Sub-iterations Second Order in Time

The TURNS code uses Newton sub-iterations to reduce linearization and factorization errors. The mathematics of the sub-iterations second order in time is described here.

A second order accurate in time solution is given by:

$$\frac{\frac{3}{2}Q^{n+1} - 2Q^n + \frac{1}{2}Q^{n-1}}{\Delta\tau} + E^{n+1}_\xi + F^{n+1}_\eta + G^{n+1}_\zeta = 0 \quad (A.27)$$

where linearization gives:

$$\begin{aligned} E^{n+1} &= E^n + \left(Q^{n+1} - Q^n\right)A^n \\ F^{n+1} &= F^n + \left(Q^{n+1} - Q^n\right)B^n \\ G^{n+1} &= G^n + \left(Q^{n+1} - Q^n\right)C^n \end{aligned} \quad (A.28)$$

Thus:

$$\left[\frac{3}{2}I + \Delta\tau\left(A^n_\xi + B^n_\eta + C^n_\zeta\right)\right]\left(Q^{n+1} - Q^n\right)$$

$$= -\Delta\tau\left(\frac{-\frac{1}{2}Q^n + \frac{1}{2}Q^{n-1}}{\Delta\tau} + E^n_\xi + F^n_\eta + G^n_\zeta\right) \quad (A.29)$$

This is modified to:

$$\left[I + \frac{2}{3}\Delta\tau\left(A^n_\xi + B^n_\eta + C^n_\zeta\right)\right]\left(Q^{n+1} - Q^n\right)$$

$$= -\Delta\tau\frac{2}{3}\left(\frac{-\frac{1}{2}Q^n + \frac{1}{2}Q^{n-1}}{\Delta\tau} + E^n_\xi + F^n_\eta + G^n_\zeta\right) \quad (A.30)$$

After applying flux-splitting, factorization and Newton sub-iterations:

$$\left[I + \frac{2}{3}\Delta\tau\left(D^P + L^P\right)\right]\left[I + \frac{2}{3}\Delta\tau\left(D^P\right)\right]^{-1}$$

$$\times\left[I + \frac{2}{3}\Delta\tau\left(D^P + U^P\right)\right]\left(Q^{p+1} - Q^p\right) \quad (A.31)$$

$$= -\Delta\tau\frac{2}{3}\left(\frac{-\frac{3}{2}Q^P - 2Q^n + \frac{1}{2}Q^{n-1}}{\Delta\tau} + E^n_\xi + F^n_\eta + G^n_\zeta\right)$$

Appendix B

Comparison of Experimental and Computational Results

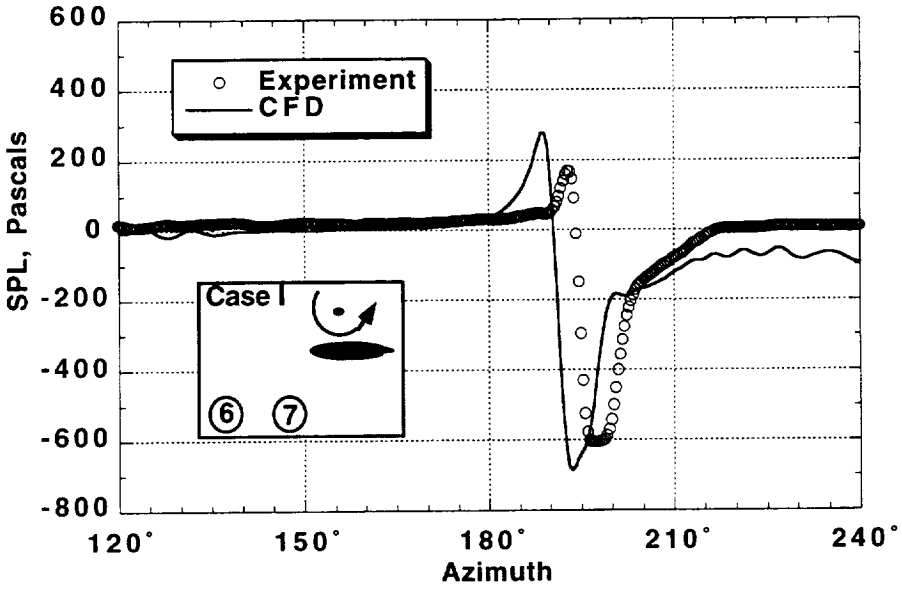

Figure B.1(a) Case I, M_{tip} = 0.6, microphone 6.

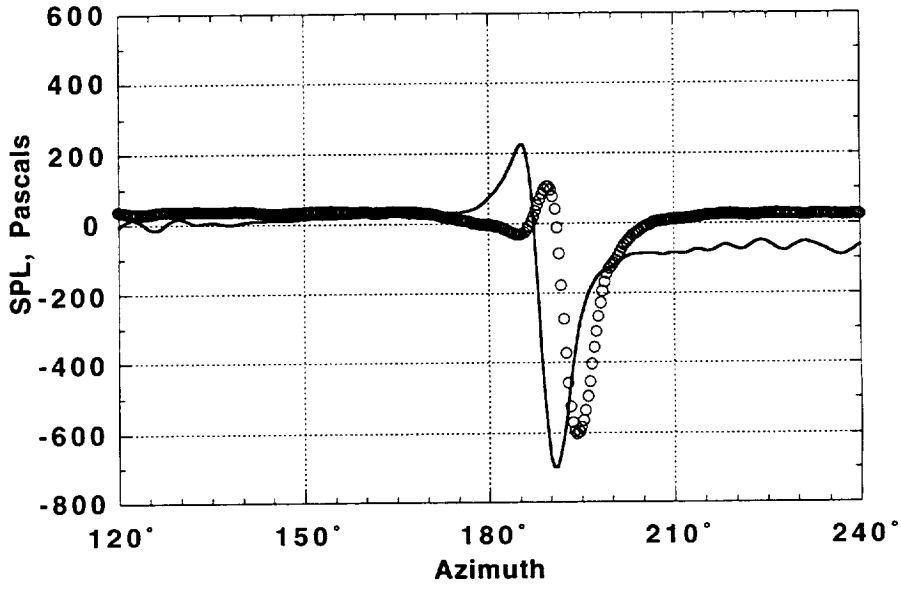

Figure B.1(b) Case I, M_{tip} = 0.6, microphone 7.

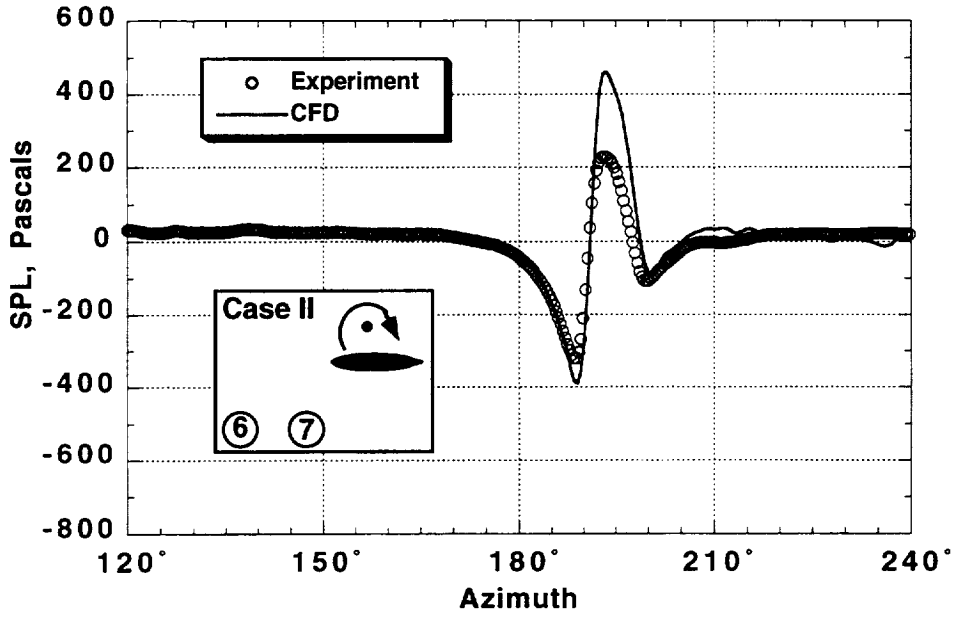

Figure B.2(a) Case II, M_{tip} = 0.6, microphone 6.

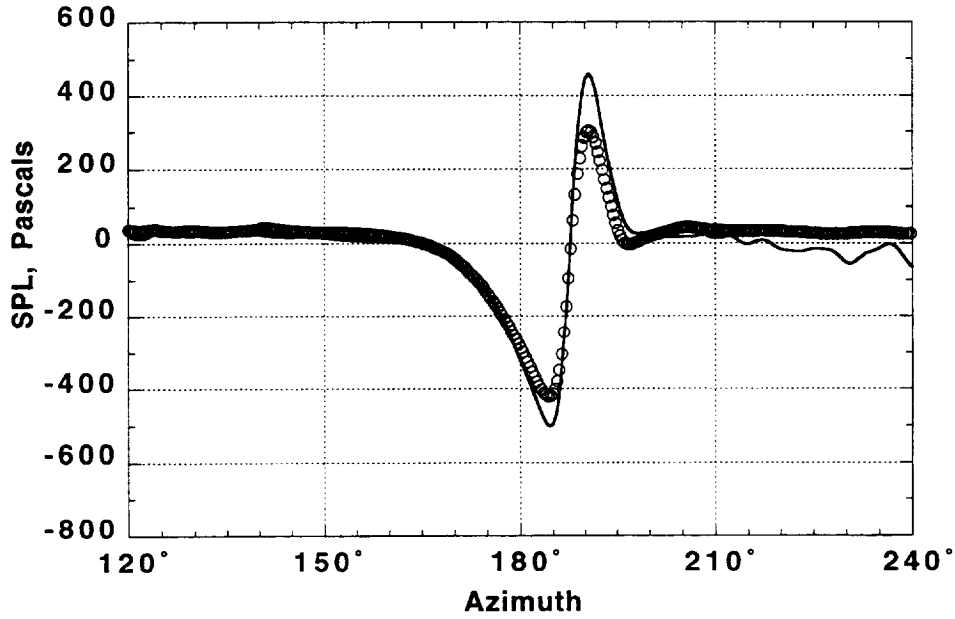

Figure B.2(b) Case II, M_{tip} = 0.6, microphone 7.

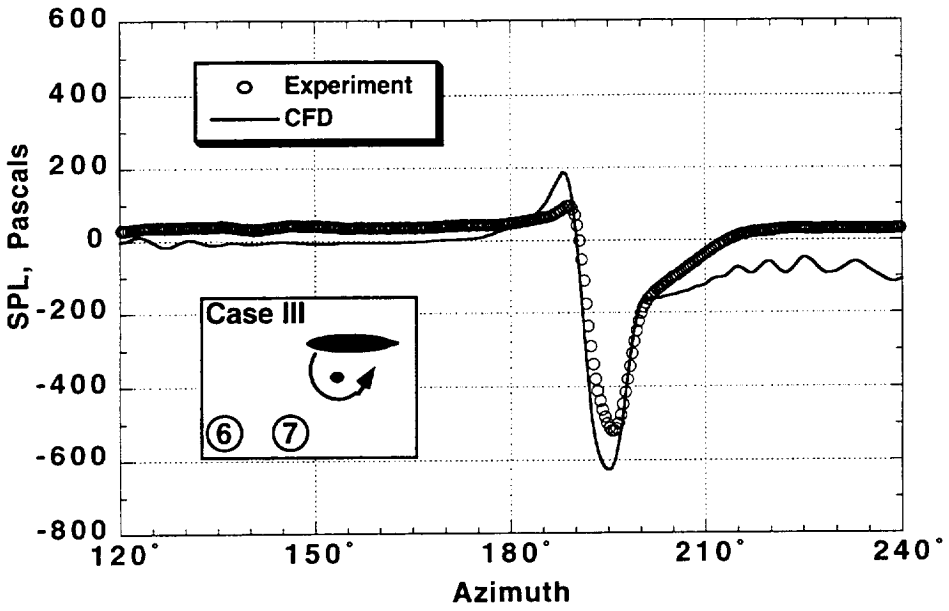

Figure B.3(a) Case III, M_{tip} = 0.6, microphone 6.

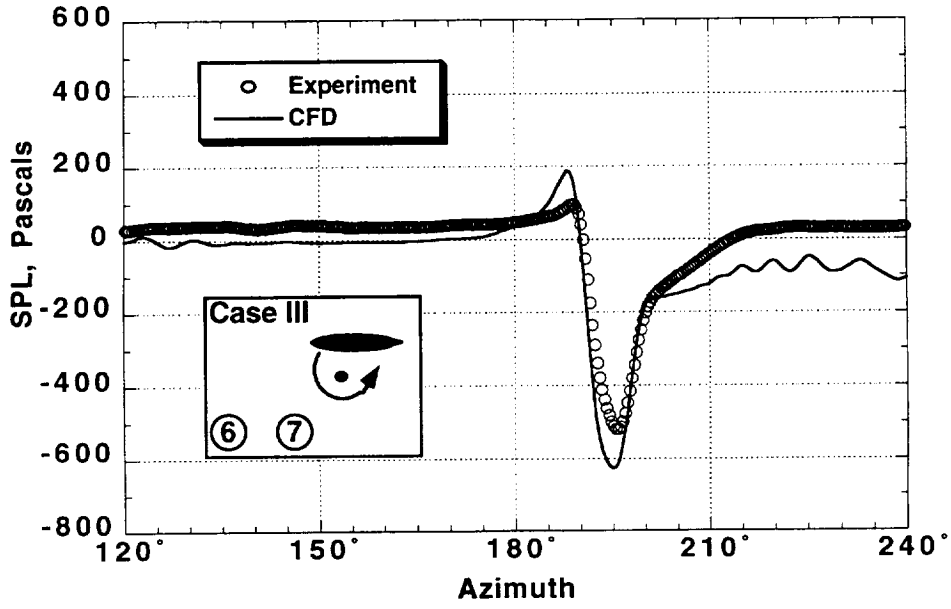

Figure B.3(b) Case III, M_{tip} = 0.6, microphone 6.

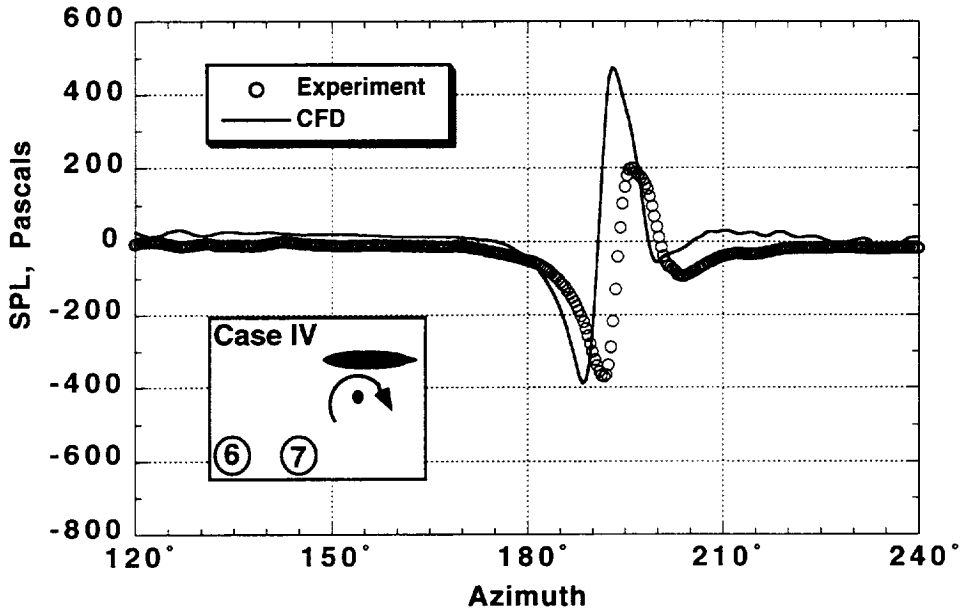

Figure B.4(a) Case IV, M_{tip} = 0.6, microphone 6.

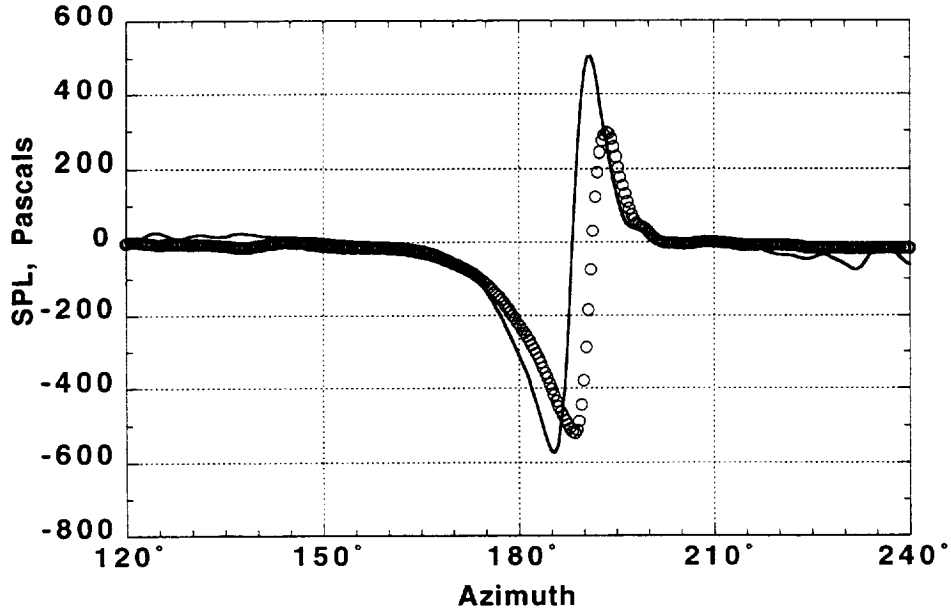

Figure B.4(b) Case IV, M_{tip} = 0.6, microphone 7.

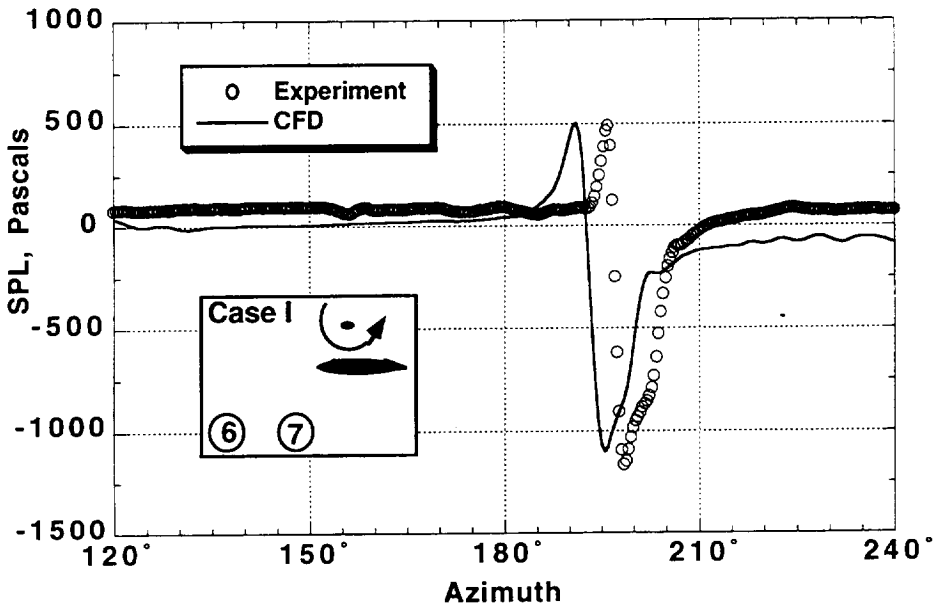

Figure B.5(a) Case I, M_{tip} = 0.7, microphone 6.

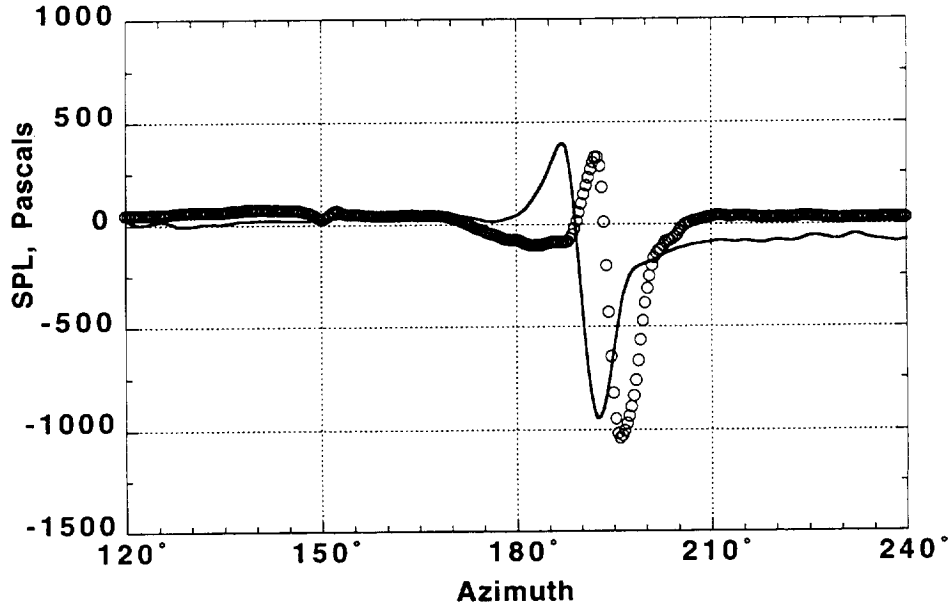

Figure B.5(b) Case I, M_{tip} = 0.7, microphone 7.

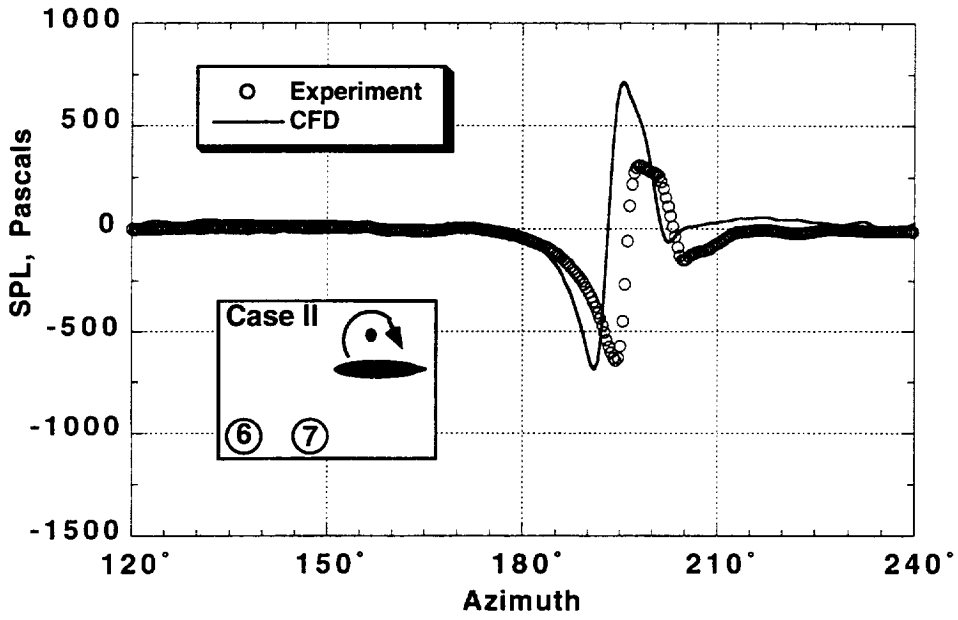

Figure B.6(a) Case II, M_{tip} = 0.7, microphone 6.

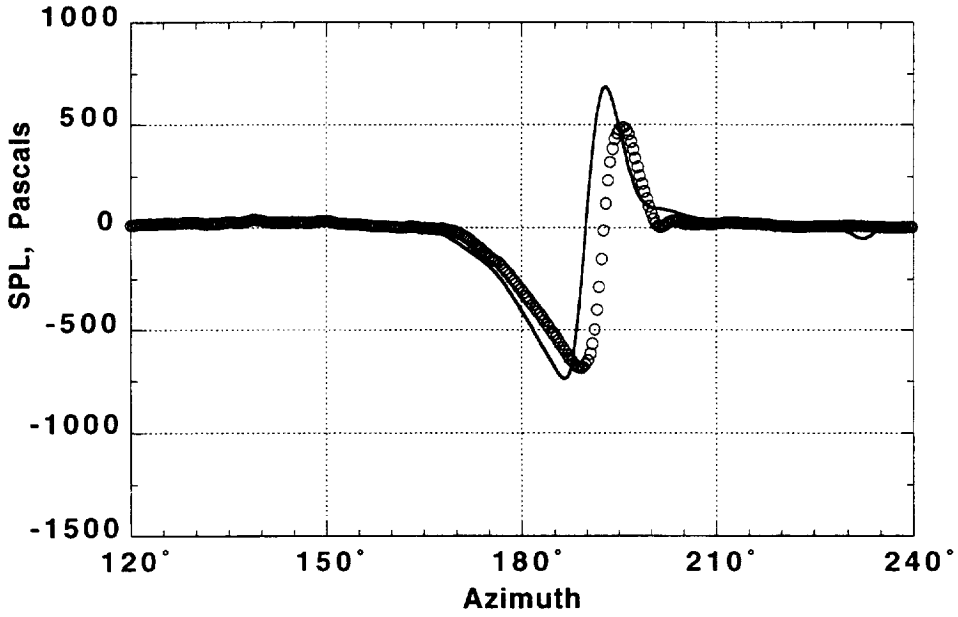

Figure B.6(b) Case II, M_{tip} = 0.7, microphone 7.

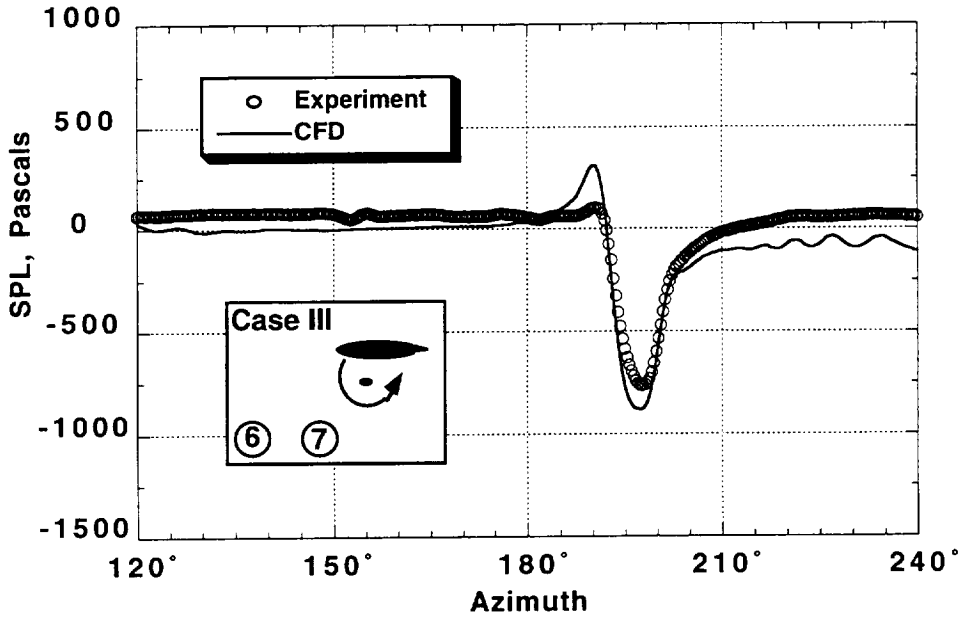

Figure B.7(a) Case III, M_{tip} = 0.7, microphone 6.

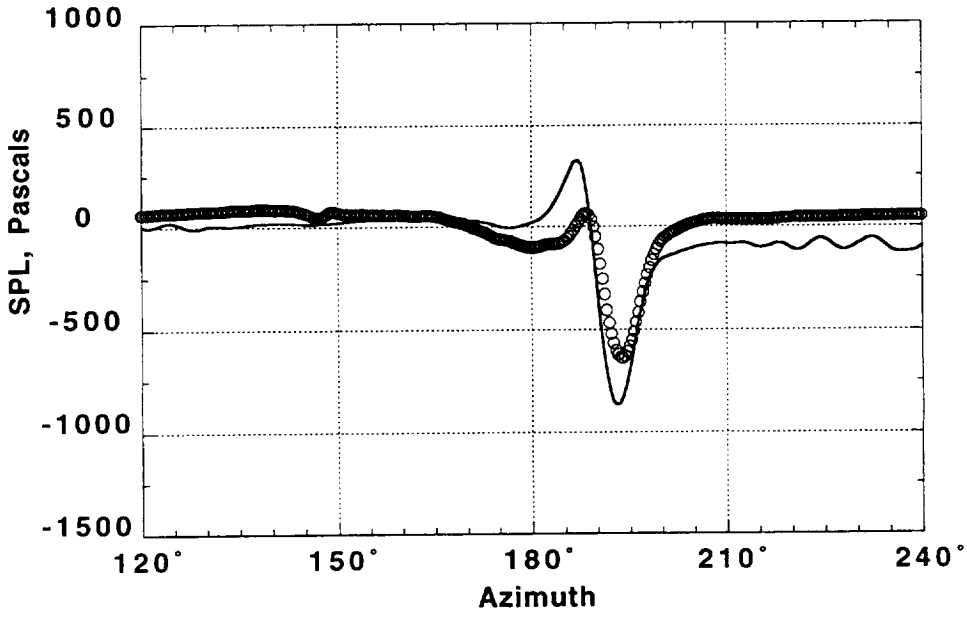

Figure B.7(b) Case III, M_{tip} = 0.7, microphone 7.

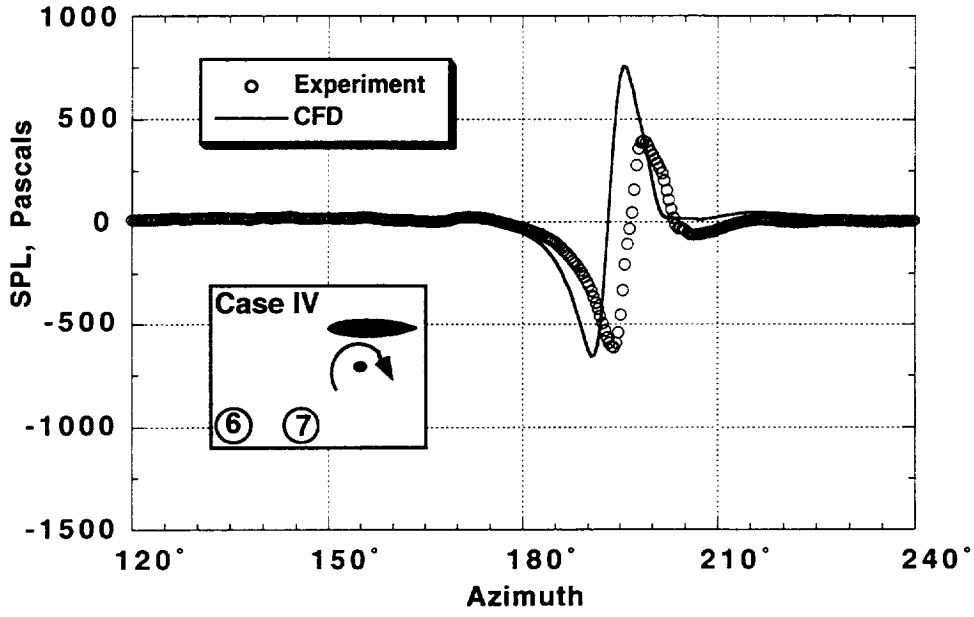

Figure B.8(a) Case IV, M_{tip} = 0.7, microphone 6.

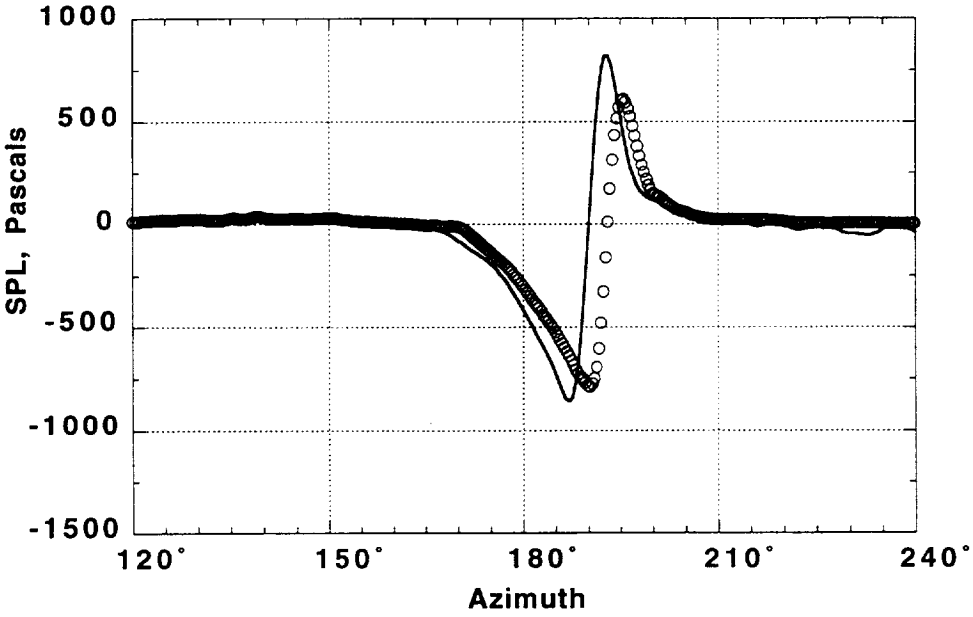

Figure B.8(b) Case IV, M_{tip} = 0.7, microphone 7.

References

1. Johnson, W.: Helicopter Theory. Princeton University Press, Princeton, N.J., 1980.
2. Schmitz, F. H.: Aeroacoustics of Flight Vehicles: Theory and Practice. Vol. I. NASA RP-1258, Aug. 1991, pp. 65–149.
3. JanakiRam, R. D.: Aeroacoustics of Rotorcraft. AGARD FDP Special Course, 1990.
4. Fradenburg, Evan A.: Aerodynamic Design of the Sikorsky S-76 Helicopter. 34th Annual Forum American Helicopter Society, Washington, D.C., May 15–17, 1978.
5. Caradonna, F. X; Strawn, R.; and Bridgeman, J. O.: An Experimental and Computational Study of Rotor-Vortex Interactions. Vertica, vol. 12, no. 4, 1988.
6. Leverton, J. W.; and Taylor, F. W.: Helicopter Blade Slap. Journal of Sound and Vibration, vol. 4., Nov. 1966.
7. Schmitz, F. H.; and Boxwell, D. A.: In flight Far-Field Measurement of Helicopter Impulsive Noise. Journal of the American Helicopter Society, vol. 21, no. 4, Oct. 1976, pp. 2–16.
8. Boxwell, D. A.; and Schmitz, F. H.: Full-Scale Measurements of Blade-Vortex Interaction Noise. Journal of the American Helicopter Society, vol. 27, no. 4, Oct. 1982, pp. 11–27.
9. Signor, D. B.; Watts, M. E.; Hernandez, F. J.; and Felker, F. I.: Blade-Vortex Interaction Noise: A Comparison of In-Flight, Full-Scale, and Small-Scale Measurements. American Helicopter Society Aeromechanics Specialists Conference, San Francisco, Calif., Jan. 1994.
10. Martin, R. M.; and Splettstoesser, W. R.: Blade-Vortex Interaction Acoustic Results from a 40% Model Rotor in the DNW. Journal of the American Helicopter Society, vol. 33, no. 1, Jan. 1988.
11. Boxwell, D. A.; Schmitz, F. H.; Splettstoesser, W. R.; and Schultz, K. J.: Helicopter Model Rotor-Blade Vortex Interaction Impulsive Noise: Scalability and Parametric Variations. Journal of the American Helicopter Society, vol. 32, no. 1, Jan. 1987, pp. 3–12.
12. Kube, R.; Splettstoesser, W. R.; Wagner, W.; Seelhorst, U.; Yu, Y.; Boutier, A.; Prieur, J.; and Mercker, E.: Initial Results from the Higher Harmonic Control Aeroacoustic Rotor Test (HART) in the German-Dutch Wind Tunnel. Paper No. 25, The 75th Fluid Dynamics Symposium, AGARD, Berlin, Germany, Oct. 1994.
13. McCormick, B. W.; and Surendraiah, M.: A Study of Rotor Blade-Vortex Interactions. The 26th Annual Forum of the American Helicopter Society, Washington, D.C., June 1970.
14. Horner, M. B.; Saliveros, E.; Kokkalis, A.; and Galbraith, R. A.: Results from a Set of Low Speed Blade-Vortex Interaction Experiments. Experiments in Fluids, vol. 14, Apr. 1993, pp. 341–352.
15. Caradonna, F. X.; Lautenschlager, J.; and Silva, M.: An Experimental Study of Rotor Blade-Vortex Interations. AIAA Paper 88-0045, Reno, Nev., Jan. 1988.
16. Caradonna, F. X.; Laub, G. H.; and Tung, C.: An Experimental Investigation of Parallel Blade-Vortex Interaction. NASA TM-86005, Nov. 1984.
17. Kitaplioglu, C.; and Caradonna, F. X.: Aerodynamics and Acoustics of Blade-Vortex Interaction using an Independently Generated Vortex. American Helicopter Society Aeromechanics Specialists Conference, San Francisco, Calif., Jan. 1994.
18. Kitaplioglu, C.; and Caradonna, F. X.: A Study of Blade-Vortex Interaction Aeroacoustics utilizing an Independently Generated Vortex. AGARD Symposium, Berlin, Germany, Oct. 1994.
19. Widnall, S. E.: Helicopter Noise Due to Blade-Vortex Interactions. Journal of the Acoustical Society of America, vol. 50, no. 1 (2), 1971, pp. 354–365.
20. Piziali, R. A.; and Du Walt, F. A.: Method for Computing Rotary Wing Airload Distribution in Forward Flight. USATRECOM TR-62-44, Nov. 1962.
21. Dat, R.: Representation of a Lifting Line in an Arbitrary Motion by a Line of Acceleration Doublets. NASA TT F-12952, May 1970.

22. Johnson, W.: A Comprehensive Analytical Model of Rotorcraft Aeromechanics and Dynamics. Part I, Analysis and Development. NASA TM-81182, June 1980.

23. Summa, J. M.: Potential Flow about 3-Dimensional Lifting Configurations with Applications to Wings and Rotors. AIAA Paper 75-126, Jan. 1975.

24. Caradonna, F. X. and Isom, M. P.: Subsonic and Transonic Potential Flow over Helicopter Rotor Blades. AIAA Journal, vol. 10, no. 12, Dec. 1972, pp. 1606–1612.

25. Arieli, R.; and Tauber, M. E.: Computation of Subsonic and Transonic Flow over Lifting Rotor Blades. AIAA Paper 79-1667, Aug. 1979.

26. Sankar, N. L.; Wake, B. E.; and Lekoudis, S. G.: Solution of the Unsteady Euler Equations for Fixed and Rotary-Wing Configurations. Journal of Aircraft, vol. 23, no. 4, Apr. 1986.

27. Wake, B. E.; and Sankar, N. L.: Solutions of the Navier–Stokes Equations for the Flow About a Rotor Blade. Journal of the American Helicopter Society, vol. 34, no. 2, Apr. 1989.

28. Lighthill, M. J.: On Sound Generated Aerodynamically. Philisophical Transactions of the Royal Society, A564, 1952.

29. Ffowcs Williams, J. E.; and Hawkings, D.;L.: Sound Generated by Turbulence and Surfaces in Arbitrary Motion. Philisophical Transactions of the Royal Society, A264, 1969.

30. Brentner, K. S.: Prediction of Helicopter Rotor Discrete Frequency Noise. NASA TM-87721, Oct. 1986.

31. Farassat, F.; and Brentner, K. S.: The Influence of Quadrupole Sources in the Boundary Layer and Wake of a Blade on Helicopter Rotor Noise. International Specialists Meeting. Philadelphia, Pa., Oct. 1991.

32. Gallman, J. M.: The Validation and Application of a Rotor Acoustic Prediction Computer Program. Army Scientific Conference Proceedings, vol. II, June 1990, pp. 1–15.

33. Isom, M.; and Purcell, T. W.: Geometrical Acoustics and Transonic Sound. AIAA Paper 87-2748 Sunnyvale, Calif., 1987.

34. Baeder, J. D.: The Computation and Analysis of Acoustic Waves in Transonic Airfoil-Vortex Interactions. Ph.D. Thesis, Sept. 1989.

35. Srinivasan, G. R.; and McCroskey, W. J.: Numerical Simulations of Unsteady Airfoil-Vortex Interactions. Vertica, vol. 11, no. 1/2, 1987, pp. 3–28. (Also, Srinivasan, G. R.: Computations of Two-Dimensional Airfoil-Vortex Interactions. NASA CR-3885, May 1985.)

36. Srinivasan, G. R.; Baeder, J. D.; Obayashi, S.; and McCroskey, W. J.: Flowfield of a Lifting Rotor in Hover - A Navier–Stokes Simulation. AIAA Journal, vol. 30, no. 10, Oct. 1992, pp. 2371–2378.

37. Srinivasan, G. R.: A Free-Wake Euler and Navier–Stokes CFD Method and Its Applications to Helicopter Rotors Including Dynamic Stall. JAI Associates, Inc., JAIA-TR-93-01, Nov. 1993.

38. Srinivasan, G. R.; and Baeder, J. D.: TURNS: A Free-Wake Euler/Navier–Stokes Numerical Method for Helicopter Rotors: AIAA Journal, vol. 31, no. 5, May 1993, pp. 959–962.

39. Baeder, J. D.; and Srinivasan, G. R.: Computational Aeroacoustic Study of Isolated Blade-Vortex Interaction Noise: American Helicopter Society Aeromechanics Specialists Conference, San Francisco, Calif., Jan. 1994.

40. Zell, Peter T.: Performance and Test Section Flow Characteristics of the National Full-Scale Aerodynamics Complex 80- by 120-Foot Subsonic Wind Tunnel. NASA TM-103920 Jan. 1993.

41. McAlister, K. W.; and Takahashi, R. K.: NACA 0015 Wing Pressure and Trailing Vortex Measurements. NASA TP-3151, AVSCOM TR 91-A-003, 1991.

42. Watts, M. E.: ALDAS User's Manual. NASA TM-102831, Apr. 1991.

43. Watts, M. E.; and St. Jean, M. M.: Data Acquisition on a Macintosh. American Helicopter Society Specialists Meeting, Philadelphia, Pa., Oct. 1991.

44. McCluer, M. S.; Baeder, J. D.; and Kitaplioglu, C.: Comparison of Experimental Blade-Vortex Interaction Noise with Computational Fluid Dynamic Calculations. American Helicopter Society Annual Forum, Fort Worth, Tex., May 1995.

45. Srinivasan, G. R.; and McCroskey, W. J.: Euler Calculations of Unsteady Interaction of Advancing Rotor with a Line Vortex. AIAA Journal, vol. 31, no. 9, Sept. 1993, pp. 1659–1666.

46. Srinivasan, G. R.; McCroskey, W. J.; and Baeder, J. D.: Aerodynamics of Two-Dimensional Blade-Vortex Interaction. AIAA Journal, vol. 24, no. 10, Oct. 1986, pp. 1569–1576.

47. Scully, M. P.: Computation of Helicopter Rotor Wake Geometry and Its Influence on Rotor Harmonic Airloads. Massachusetts Institute of Technology, ASRL TR 178-1, Mar. 1975.

48. Roe, P. L.: Approximate Riemann Solvers, Parameter Vectors, and Difference Schemes. Journal of Computational Physics, vol. 43, no. 3, 1981, pp. 357–372.

49. Anderson, W. K; Thomas, J. L.; and van Leer, B.: A Comparison of Finite Volume Flux Vector Splittings for the Euler Equations. AIAA Paper 85-0122, Jan. 1985.

50. Jameson, A.; and Yoon, S.: Lower-Upper Implicit Schemes with Multiple Grids for the Euler Equations. AIAA Journal, vol. 25, no. 7, 1987, pp. 929–935.

51. Koren, B.: Upwind Schemes, Multigrid and Defect Correction for the Steady Navier–Stokes Equations. International Conference on Numerical Methods in Fluid Dynamics, Springer-Verlag, Berlin 1989.

REPORT DOCUMENTATION PAGE

Form Approved
OMB No. 0704-0188

1. AGENCY USE ONLY *(Leave blank)*	2. REPORT DATE	3. REPORT TYPE AND DATES COVERED
	December 1996	Technical Memorandum

4. TITLE AND SUBTITLE

Helicopter Blade-Vortex Interaction Noise with Comparisons to CFD Calculations

5. FUNDING NUMBERS

505-59-36

6. AUTHOR(S)

Megan S McCluer

7. PERFORMING ORGANIZATION NAME(S) AND ADDRESS(ES)

Ames Research Center
Moffett Field, CA 94035-1000

8. PERFORMING ORGANIZATION REPORT NUMBER

A-962847

9. SPONSORING/MONITORING AGENCY NAME(S) AND ADDRESS(ES)

National Aeronautics and Space Administration
Washington, DC 20546-0001

10. SPONSORING/MONITORING AGENCY REPORT NUMBER

NASA TM-110423

11. SUPPLEMENTARY NOTES

Point of Contact: Megan S McCluer, Ames Research Center, MS T12-B, Moffett Field, CA 94035-1000
(415) 604-0010

12a. DISTRIBUTION/AVAILABILITY STATEMENT

Unclassified — Unlimited
Subject Category 71

12b. DISTRIBUTION CODE

13. ABSTRACT ***(Maximum 200 words)***

A comparison of experimental acoustics data and computational predictions was performed for a helicopter rotor blade interacting with a parallel vortex. The experiment was designed to examine the aerodynamics and acoustics of parallel blade-vortex interaction (BVI) and was performed in the Ames Research Center (ARC) 80- by 120-Foot Subsonic Wind Tunnel. An independently generated vortex interacted with a small-scale, nonlifting helicopter rotor at the 180 deg azimuth angle to create the interaction in a controlled environment. Computational fluid dynamics (CFD) was used to calculate near-field pressure time histories. The CFD code, called Transonic Unsteady Rotor Navier–Stokes (TURNS), was used to make comparisons with the acoustic pressure measurement at two microphone locations and several test conditions. The test conditions examined included hover tip Mach numbers of 0.6 and 0.7, advance ratio of 0.2, positive and negative vortex rotation, and the vortex passing above and below the rotor blade by 0.25 rotor chords. The results show that the CFD qualitatively predicts the acoustic characteristics very well, but quantitatively overpredicts the peak-to-peak sound pressure level by 15 percent in most cases. There also exists a discrepancy in the phasing (about 4 deg) of the BVI event in some cases. Additional calculations were performed to examine the effects of vortex strength, thickness, time accuracy, and directionality. This study validates the TURNS code for prediction of near-field acoustic pressures of controlled parallel BVI.

14. SUBJECT TERMS

Blade-vortex interaction, BVI, Computational fluid dynamics, CFD, Helicopter noise, TURNS, Helicopter acoustics

15. NUMBER OF PAGES

54

16. PRICE CODE

A04

17. SECURITY CLASSIFICATION OF REPORT	18. SECURITY CLASSIFICATION OF THIS PAGE	19. SECURITY CLASSIFICATION OF ABSTRACT	20. LIMITATION OF ABSTRACT
Unclassified	Unclassified		